Cell Reports

Article

Cecal necroptosis triggers lethal cardiac dysfunction in TNF-induced severe SIRS

Graphical abstract

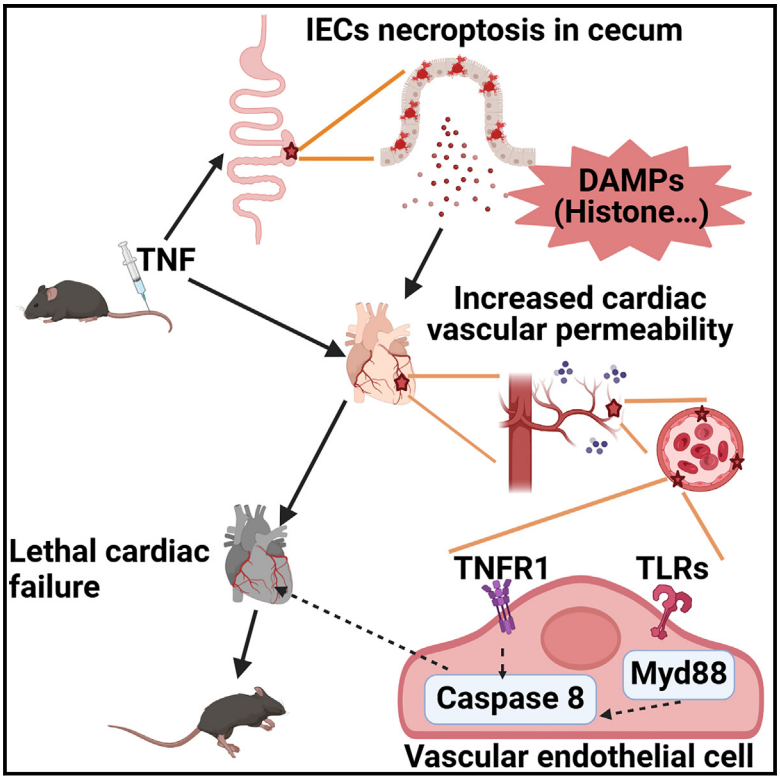

Highlights

- Necroptosis in the cecum initiates a fatal process in TNF-treated mice
- Synergy of TNF and DAMPs from necroptotic cecal cells causes cardiac damage
- Myd88-caspase-8 signaling in cardiac endothelial cells elicits diastolic dysfunction
- The death of TNF-treated mice results from diastolic heart failure

Authors

Jianfeng Wu, Tingting Ai, Peng He, ..., Suqin Wu, Wanze Chen, Jiahuai Han

Correspondence

jhan@xmu.edu.cn

In brief

Excessive TNF-induced severe SIRS serves as a model for animal death caused by multiple organ failure. Wu et al. find that DAMPs released from TNF-induced necroptotic cecum epithelial cells, in synergy with TNF, trigger Myd88-dependent caspase-8 activation in cardiac endothelial cells, leading to deteriorating diastolic function and, ultimately, mouse death.

Wu et al., 2024, Cell Reports *43*, 114778
October 22, 2024 © 2024 Published by Elsevier Inc.
https://doi.org/10.1016/j.celrep.2024.114778

CellPress

Cell Reports

CellPress
OPEN ACCESS

Article

Cecal necroptosis triggers lethal cardiac dysfunction in TNF-induced severe SIRS

Jianfeng Wu,[1,2,6] Tingting Ai,[1,6] Peng He,[1,5] Qilin Shi,[1] Yangxin Li,[1] Ziguan Zhang,[3] Minwei Chen,[3] Zhengrong Huang,[3] Suqin Wu,[2] Wanze Chen,[4] and Jiahuai Han[1,2,5,7,*]

[1]State Key Laboratory of Cellular Stress Biology, Xiamen University, Xiamen, Fujian 361102, China
[2]Laboratory Animal Research Center, Xiamen University, Xiamen, Fujian 361102, China
[3]Xiamen Key Laboratory of Cardiac Electrophysiology, The First Affiliated Hospital of Xiamen University, Xiamen, Fujian 361102, China
[4]CAS Key Laboratory of Quantitative Engineering Biology, Shenzhen Institute of Advanced Technology, Shenzhen, Guangdong 518000, China
[5]Research Unit of Cellular Stress of Chinese Academy of Medical Sciences, Xiang'an Hospital of Xiamen University, Xiamen, Fujian 361102, China
[6]These authors contributed equally
[7]Lead contact
*Correspondence: jhan@xmu.edu.cn
https://doi.org/10.1016/j.celrep.2024.114778

SUMMARY

Tumor necrosis factor (TNF) induces systemic inflammatory response syndrome (SIRS), and severe SIRS can serve as a model for studying animal death caused by organ failure. Through strategic cecectomy, we demonstrate that necroptosis in the cecum initiates the death process in TNF-treated mice, but it is not the direct cause of death. Instead, we show that it is the cardiac dysfunction downstream of cecum damage that ultimately leads to the death of TNF-treated mice. By *in vivo* and *ex vivo* physiological analyses, we reveal that TNF and the damage-associated molecular patterns (DAMPs) released from necroptotic cecal cells jointly target cardiac endothelial cells, triggering caspase-8 activation and subsequent cardiac endothelial damage. Cardiac endothelial damage is a primary cause of the deterioration of diastolic function in the heart of TNF-treated mice. Our research provides insights into the pathophysiological process of TNF-induced lethality.

INTRODUCTION

Tumor necrosis factor (TNF) is a multifunctional cytokine implicated in various biological processes, including cellular proliferation, inflammatory responses, and cell death (apoptosis and necroptosis).[1] Experimental injection of exogenous TNF induces systemic inflammatory response syndrome (SIRS), mimicking part of the acute systemic inflammation and tissue damage seen in human patients following infection, trauma, thermal injury, or surgery.[2,3]

While TNF induces inflammatory cytokines such as interleukin-6 (IL-6),[4] IL-1β,[5] IL-17,[6] and interferon (IFN)-α/β,[7] which are implicated in TNF-induced SIRS pathology, studies show that cytokine levels do not always correlate with survival in TNF-induced SIRS.[8] Instead, tissue damage has been proposed to play a significant role in TNF-induced SIRS pathology.[2,8–10]

TNF-induced tissue damage affects multiple organs, including the intestines, lungs, kidneys, and liver.[2,11] Necroptotic cell death has been identified as a crucial pathological mechanism in TNF-induced SIRS and animal death. Blocking necroptosis can diminish TNF-induced animal death,[10–12] and simultaneous impairment of apoptotic and necroptotic pathways fully protects mice from the lethal effects of TNF.[9]

The pathological role of necroptosis in TNF-induced SIRS and animal death has been studied extensively using necroptosis abolition mouse models or specific necroptosis inhibitors like necrostatin-1.[11–14] Enhanced inflammatory responses and necroptotic cell death, particularly in the liver, have been associated with exacerbation of SIRS by necroptosis, leading to increased vascular permeability, coagulation, and multi-organ dysfunction.[8,11,15] According to a recent study,[9] preventing TNF-induced mouse death was successful in $Rip3^{fl/fl}Villin^{cre/-}$ mice. This highlights the critical role of necroptosis in intestinal epithelial cells (IECs) in TNF-induced mortality. Our prior findings suggest that RIP3-dependent tissue damage, primarily in the cecum, may be vital to TNF-induced mouse death.[10]

Necroptosis releases damage-associated molecular patterns (DAMPs),[16] such as histones, which trigger inflammatory responses and correlate with mortality in sepsis patients.[17–20] Furthermore, TNF-induced dysfunction of goblet and Paneth cells has been linked to bacterial translocation and mortality in mice.[21] However, recent studies found no connection between necroptosis and intestinal permeability of microbes in TNF-treated animals.[8] While it is reasonable to assume that DAMPs from a damaged organ could affect other organs, experimental evidence supporting this hypothesis is still lacking.

This is an open access article under the CC BY-NC-ND license (http://creativecommons.org/licenses/by-nc-nd/4.0/).

Cardiac dysfunction is a common feature of SIRS-related deaths in septic shock patients,[22–24] and TNF has been reported to induce apoptosis in cultured cardiomyocytes and cardiac dysfunction *in vivo*.[25–28] However, whether these *in vitro* and *in vivo* observations share the same underlying mechanisms and how TNF induces cardiac dysfunction remains unclear.

In this study, we systematically investigated the pathological processes underlying TNF-induced mouse death and revealed a sequence of organ damage triggered by TNF treatment. Cecum IECs, the cells most sensitive to TNF-induced necroptosis, respond first to TNF and release DAMPs into circulation, mediating inter-organ signaling. The lethal damage occurs in the heart, where TNF and DAMPs synergistically damage the cardiac endothelium. TNF- and DAMP/Myd88-mediated caspase-8 activation is the major driver of endothelium damage. Thus, TNF-induced mouse death involves a pathological sequence initiated by cecal cell necroptosis, cecum-cardiac signal transfer, and the synergy of TNF and DAMPs in triggering cardiac failure.

RESULTS

Cecectomy protects mice from TNF-induced death

To better understand the pathological process of TNF-induced animal death, we studied the effects of TNF at 100% lethal dose (LD_{100}) in C57BL/6J mice. At LD_{100}, *Rip3* deficiency prevented mice from TNF-induced death (Figure S1A). Additionally, the toxic effects triggered by TNF, such as rapid submucosal edema in the cecum and abundant cecal epithelial cell destruction and shedding observed in wild-type mice, were significantly attenuated in $Rip3^{-/-}$ mice.[10] Similar results were observed when $Mlkl^{-/-}$ mice were used (Figures S1B and S1C). Phosphorylation of MLKL on serine 345 (p-MLKL), an essential event in necroptosis,[29] was detected in cecal epithelial cells in wild-type mice but not in $Mlkl^{-/-}$ mice after TNF injection (Figure S1D). We confirmed here that TNF induces necroptotic cell death in cecal epithelial cells.

To investigate the role of cecal epithelial cell necroptosis in TNF-induced lethality, we performed cecectomy on wild-type mice.[30] Mice that underwent the same surgical procedure without ileocecal junction ligation or cecal excision were used as the sham group. Mice that underwent cecectomy and sham mice exhibited similar behaviors and lifespans (Figures S1E and S1F). Cecectomy prevented mice from TNF-induced death and ameliorated hypothermia induced by TNF (Figure 1A). In contrast, cecectomy had no protective effect on lipopolysaccharide (LPS)-induced mouse death (Figures S1G and S1H). This is consistent with data showing that TNF-induced necroptosis preferentially damages the cecum, while LPS targets multiple organs/tissues and cells.[31,32]

To determine whether the protective effects of cecectomy against TNF-induced death were due to the abrogation of cecal necroptosis, $Mlkl^{-/-}$ mice and their wild-type littermates were subjected to cecectomy or sham surgery and treated with TNF. TNF-induced hypothermia and death were alleviated in wild-type and $Mlkl^{-/-}$ mice that had undergone cecectomy, but *Mlkl* knockout and cecectomy did not have an additive effect in protecting against TNF-induced hypothermia or death (Figure 1B). Similar results were obtained when $Rip3^{-/-}$ mice and their wild-type littermates were used (Figure 1C). Collectively, these data demonstrate that cecal cell necroptosis is a required initiative event in TNF-induced mouse death.

The death-promoting effect of cecal cell necroptosis is not linked to the production of the major inflammatory mediators or intestinal bacterial translocation

TNF is a well-known proinflammatory cytokine, and studies have shown that TNF-induced death is alleviated in some inflammatory cytokine-deficient mice,[4–7,33] but no correlation between inflammatory cytokine levels and TNF-induced mouse death has been reported.[8] Thus, we examined serum levels of inflammatory cytokines in TNF-treated cecectomized and sham mice. While IL-6, IL-1β, IL-18, and IFN-β levels were similar across TNF-treated mice (Figures S2A–S2D), decreased IFN-γ and IL-22 levels were observed in TNF-treated cecectomized mice (Figures S2E and S2F). To assess whether the enhanced cytokine response from the cecum correlates with mouse death, we compared cytokine levels in TNF-treated $Mlkl^{-/-}$ mice and wild-type littermates. As shown in Figures S2G–S2L, cytokine levels were comparable between the two groups. We also examined the serum levels of inflammatory lipid mediators in TNF-treated mice and found that cecectomy did not cause differences (Figures S2M–S2V). Similar results were also obtained when $Mlkl^{-/-}$ mice and their wild-type littermates were used (Figures S2W–S2AF). Thus, the protective effect of cecectomy in TNF-induced death in mice is not associated with the secretion of inflammatory mediators.

The intestinal lumen is rich in microbes, and the translocation of microbes from the cecum to the blood or abdominal cavity is widely used to model sepsis in mice.[34] Normal villous architecture with increased intraepithelial lymphocytes was observed in different small intestine sections (duodenum, ileum, and jejunum) in TNF-treated cecectomized and sham mice, and no colon damage was observed (Figure S3A). The results were the same when $Mlkl^{-/-}$ or $Rip3^{-/-}$ mice and their wild-type littermates were examined (Figures S3B and S3C). Importantly, significant pathological alterations were only observed in the cecum of wild-type mice (Figure S1C). There was an equally small number of bacterial colonies in cultured blood samples from both the sham (or wild-type) and cecectomized ($Rip3^{-/-}$ or $Mlkl^{-/-}$) groups (Figures S3D–S3F). To determine whether bacterial invasion occurs with prolonged TNF treatment, we administered TNF (LD_{50}) to $Mlkl^{-/-}$ and wild-type littermates for up to 72 h. We observed minimal bacterial invasion and no significant differences between the groups (Figure S3G). Thus, cecal epithelial cell necroptosis in TNF-treated mice in our experimental condition does not lead to the entry of microbes from the intestinal lumen into the blood that causes secondary sepsis.

Cecal cell necroptosis ultimately affects cardiac function

TNF at LD_{100} caused certain levels of interstitial pneumonia, immune cell infiltration in the lungs (Figures S4A–S4C), liver damage (alanine aminotransferase [ALT] and aspartate transferase [AST] level), and vascular permeability and coagulation in the liver, and these were not influenced by cecectomy or deletion of *Mlkl*

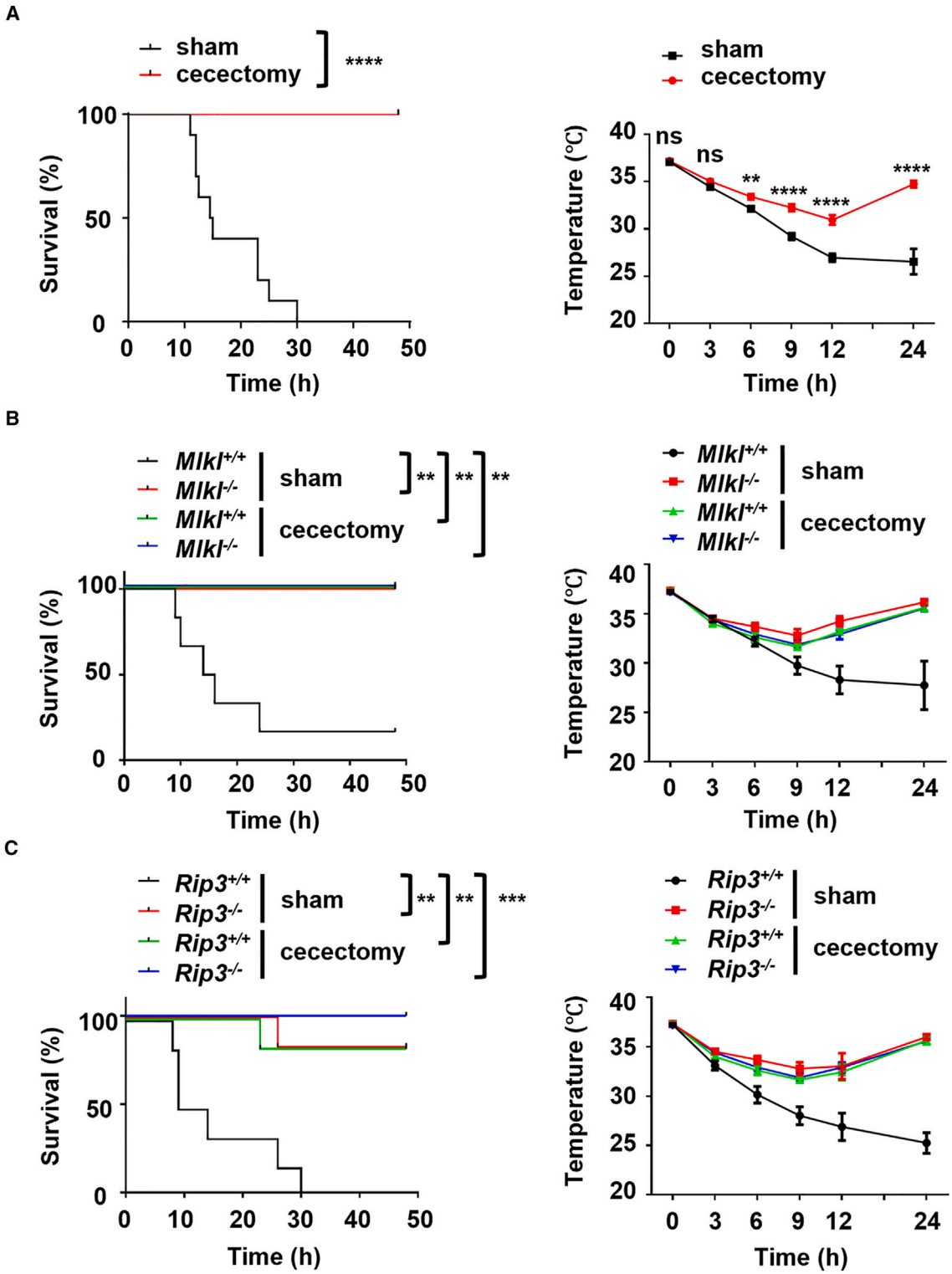

Figure 1. Cecectomy protects mice from TNF-induced death in an MLKL- or RIP3-dependent manner

(A) Cecectomized or sham wild-type mice were injected intravenously with TNF. The mortality rate and rectal temperature were recorded (n = 10).
(B and C) Same as (A) but for *Mlkl*$^{-/-}$ mice (B) and *Rip3*$^{-/-}$ mice (C) and their wild-type littermates (n = 6). Cumulative results of two or three independent experiments are shown. Each symbol represents a representative sample. The survival curve is presented as a Kaplan-Meier plot. The small horizontal lines indicate the means ± sems. ns, not significant, $P > 0.05$; * $P < 0.05$; ** $P < 0.01$; *** $P < 0.001$; **** $P < 0.0001$. The data were analyzed by two-tailed unpaired t tests. See also Figures S1.

or *Rip3* (Figures S4D–S4H). However, when the cardiac system was examined, the difference was apparent. Lead II electrocardiography (ECG) showed continuous deterioration of cardiac function in TNF-treated sham mice, as indicated by a prolonged electrocardiographic interval, a widened QRS complex, and ST elevation in the late stage (8 h) (Figure 2A). No obvious electrocardiographic cycle signals were recorded in moribund mice. Significant improvement in cardiac function was observed by ECG in TNF-treated cecectomized mice, and the lead II ECG waveform almost returned to normal 24 h after TNF injection (Figure 2A). Consistent with these findings, echocardiography revealed significant improvement in cardiac function in TNF-treated mice that had undergone cecectomy (Figure 2B; Video S1). We calculated the left ventricle (LV) volume in the diastole stage and found that the LV volume decreased continuously in sham mice, while this decline was mitigated in cecectomized mice at 6 h and 9 h (Figure 2C). Similar results were obtained for cardiac output (CO) (Figure 2C). Moreover, a weak heartbeat and continuous decreases in LV volume and CO were also observed in TNF-injected wild-type mice, and these changes were also strongly ameliorated in their *Mlkl*$^{-/-}$ (Figures S5A–S5C) and *Rip3*$^{-/-}$ (Figures S5E–S5G) littermates. We also found that the intact ventricular septum (IVS) and left ventricular posterior wall (LVPW) during the systole stage thickened after TNF injection (Figure 2D). Although cecectomy alleviated these changes, deletion of *Mlkl* or *Rip3* slightly affects the TNF-induced increase of the thickness of the IVS and LVPW (Figures S5D and S5H), suggesting that the changes in IVS and LVPW were not related to cecum necroptosis. When LV and CO values in a number of mice that were undergoing survival or death were compared, it appears that there might be a threshold level of LV and CO for survival (Figure S5I). Collectively, cecum epithelial cell necroptosis exacerbated TNF-induced cardiac dysfunction in mice, and the level of the reduced CO could be a criterion for forewarning of mouse death, consistent with studies demonstrating that decreased CO can represent cardiac dysfunction and predict mortality in septic mice or clinical patients.[22,23,35]

When cardiomyocytes were compared, no obvious cardiac structural changes were observed between TNF-treated cecectomized and sham mice (Figure S6A) and between TNF-treated *Mlkl*$^{-/-}$ (Figure S6B) or *Rip3*$^{-/-}$ (Figure S6C) mice and their wild-type littermates. TNF treatment increased serum cardiac troponin I levels, a biomarker of cardiomyocyte damage, but cecectomy had no significant effect compared to sham mice (Figure S6D). Histopathological analysis revealed an increased space between the cardiomyocytes, and cecectomy did not affect this change. Local edema and vacuoles were observed in a small number of cardiomyocytes in the sham mice, and these changes were slightly attenuated by cecectomy (Figure S6E). In addition, cardiomyocyte size, measured by wheat germ agglutinin staining, was slightly increased 6 h after TNF injection, but no differences were observed between the sample and control mice (Figure S6F). Additionally, TNF treatment did not cause significant changes in cardiac electrolyte (Na^+, K^+, and bicarbonate) levels between cecectomy and sham mice or between *Mlkl*$^{-/-}$ and their wild-type littermates (Figure S6G). ATP production was significantly decreased by TNF treatment, but no differences were observed between *Mlkl*$^{-/-}$ and their wild-type littermates (Figure S6H). Moreover, mice with *Tnfr1* deletion in cardiomyocytes (*Tnfr1*$^{fl/fl}$*aMHC*$^{Cre/-}$) exhibited comparable lethality rates and cardiomyocyte damage as their wild-type littermates (*Tnfr1*$^{fl/fl}$) (Figures S6I and S6J).

Intraperitoneal injection of atropine, a prescription drug used to treat symptoms of bradycardia, efficiently prevented death in wild-type mice (Figure 2E). Atropine treatment did not affect cecal epithelial cell destruction or shedding (Figure 2F), cardiomyocyte spacing, local edema, or vacuoles (Figure 2G); however, echocardiography revealed that cardiac function was improved in atropine-treated mice (Figures 2H–2J). Besides, the cardiac function of all surviving cecectomy or atropine-treated mice 48 h after TNF (LD_{100}) administration was restored to the baseline of untreated mice (Figures S6K and S6L). The cardiac function recovery of the surviving mice was the same in LD_{50} TNF-treated mice (Figures S6M and S6N). Thus, cecum epithelial cell necroptosis is unlikely to impair cardiac function by affecting cardiomyocyte damage.

Renal injury in TNF-treated mice links to cardiac dysfunction

Significant differences in renal damage were also observed between TNF-treated wild-type mice that had undergone cecectomy and TNF-treated wild-type sham mice. As shown in Figure S7A, comparable brush border loss in tubular epithelial cells was observed in both cecectomized and sham mice 3 h after TNF injection. However, renal damage was increased at 6 and 9 h in TNF-treated sham mice, and slight dilation and vacuolization of tubular epithelial cells emerged at 9 h; in contrast, renal damage was not exacerbated at 6 h or 9 h in TNF-treated cecectomized mice. The concentration of total inorganic phosphate in serum (Figure S7B), an indicator of renal damage, showed comparable results. *Mlkl*$^{-/-}$ and *Rip3*$^{-/-}$ mice phenocopied cecectomy mice in TNF-induced renal damage and serum inorganic phosphate concentration (Figures S7C–S7F). Both cecectomy and *Mlkl* or *Rip3* deficiency significantly attenuated renal damage at a relatively late time point (9 h and 12 h) after TNF injection (Figures S7A–S7F), raising the possibility that the renal damage may be further downstream of cecal necroptosis. The kidney is sensitive to ischemic injury,[36] and cardiac dysfunction causes kidney damage.[37] Therefore, we analyzed TNF-induced renal damage in mice treated with atropine or left untreated and found that atropine administration indeed reduced renal damage (Figure S7G). Thus, renal damage in TNF-treated mice is attributed not only to cecal necroptosis but also to cardiac dysfunction.

DAMPs released from cecal cell necroptosis participate in TNF-induced mouse death

To further explore how cecal cell necroptosis exacerbates cardiac dysfunction, we analyzed the serum proteome of wild-type mice treated with or without TNF for 6 h. 2417 serum proteins were identified via mass spectrometry (Figure 3A). Among the TNF-increased proteins, six were histones. Western blotting with anti-histone 3 antibody confirmed that TNF induced an increase in the serum histone concentration, and this increase was diminished by cecectomy or *Mlkl* or *Rip3* deficiency in mice (Figures 3B–3D).

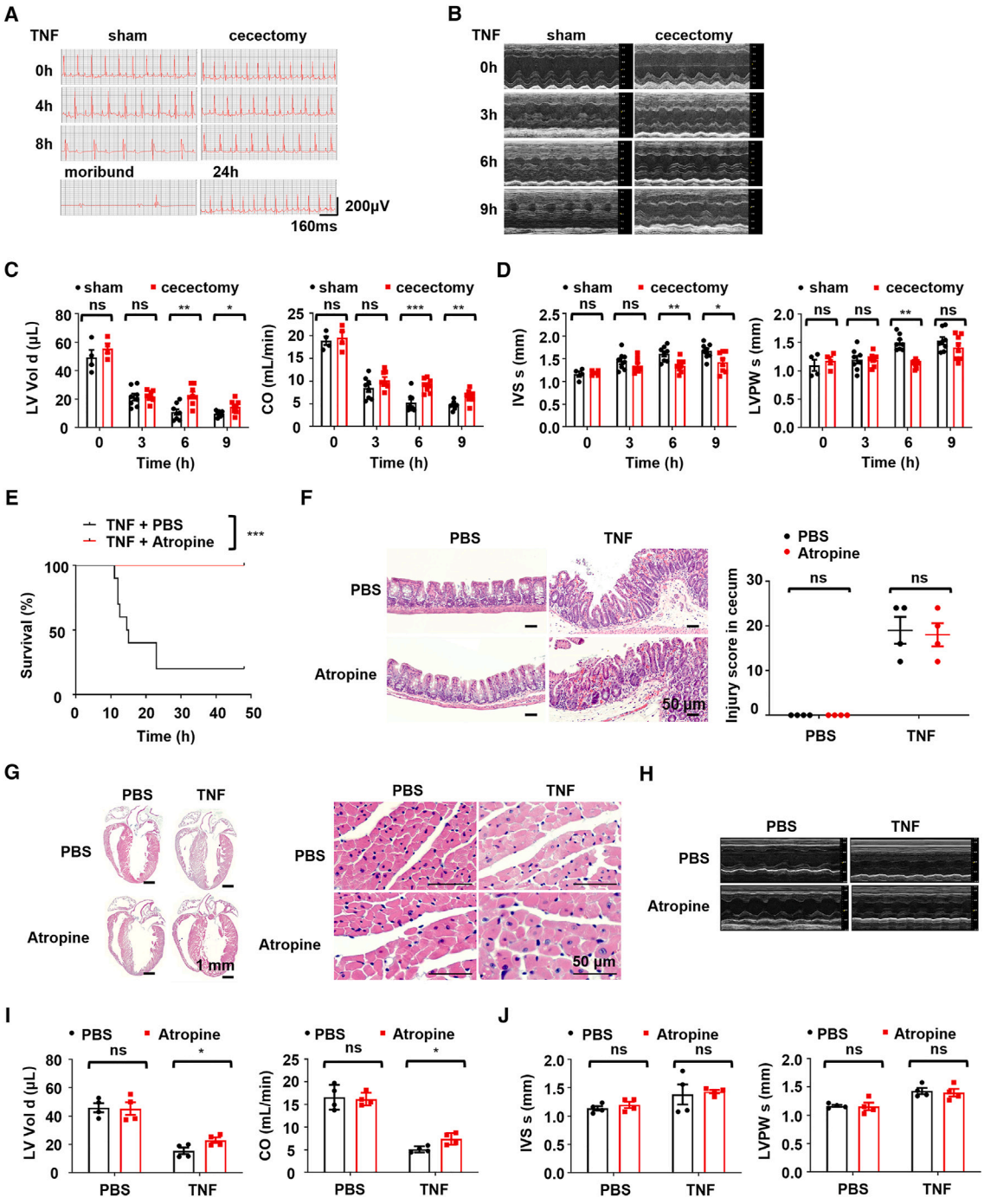

Figure 2. Cecal cell necroptosis promotes TNF-induced lethal cardiac dysfunction

(A) Electrocardiograms of TNF-treated cecectomized or sham mice at the indicated times.

(B–D) Cardiac function assessed by echocardiography: two-dimensional M mode (B), left ventricular end diastolic volume (LV vol, d) and cardiac output (CO) (C), and interventricular septum dimension in systole (IVS, s) and left ventricular posterior wall thickness in systole (LVPW, s) (D) (n = 4–8).

(E) Mortality rate in TNF-treated wild-type mice injected intraperitoneally with atropine or PBS (1 h before and 4 h after TNF) (n = 6).

(F and G) Tissue injury analysis of the cecum (F) and heart (G) in TNF-treated wild-type mice treated with atropine or PBS (n = 4).

(H and J) Cardiac function in TNF-treated wild-type mice measured by echocardiography: two-dimensional M mode (H), LV vol, d and CO (I) and IVS, s and LVPW, s (J) (n = 4).

Scale bars: 50 μm (F) and 1 mm and 50 μm (G). Cumulative results from two or three independent experiments are shown. Each symbol represents a representative sample. The survival curve is presented as a Kaplan-Meier plot. The small horizontal lines indicate the means ± sems. ns, not significant, $P > 0.05$; *, $P < 0.05$; **, $P < 0.01$; ***, $P < 0.001$; ****, $P < 0.0001$. The data were analyzed by two-tailed unpaired t tests. See also Figures S2–S7 and Video S1.

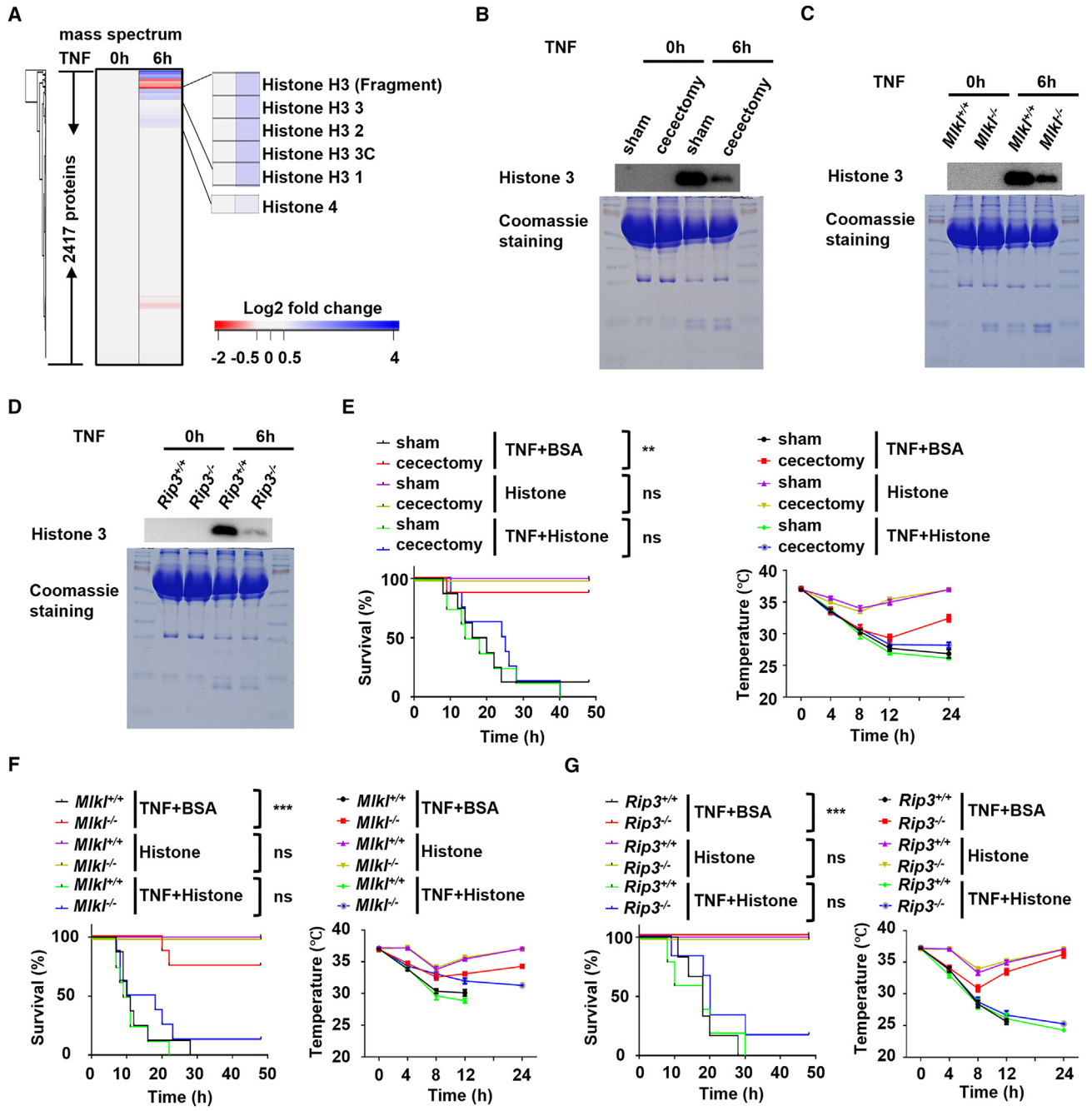

Figure 3. DAMPs released from cecal cell necroptosis promote TNF-induced mouse death

(A) Serum proteome analysis of TNF-treated wild-type mice (n = 3).

(B–D) Western blotting for histone 3 in serum samples with total serum proteins as loading control.

(E-G) TNF-treated cecectomized or sham mice (E, n = 8), *Mlkl*$^{-/-}$ mice (F, n = 8), and *Rip3*$^{-/-}$ mice (G, n = 5) and their wild-type littermates were injected with histones or BSA. Mortality rate and rectal temperature were recorded. Survival curves (Kaplan-Meier plot) and mean ± SEM are shown.

Cumulative results from two or three independent experiments are shown. Each symbol represents a representative sample. The survival curve is presented as a Kaplan-Meier plot. The small horizontal lines indicate the means ± sems. ns, not significant, $P > 0.05$; *, $P < 0.05$; **, $P < 0.01$; ***, $P < 0.001$; ****, $P < 0.0001$. The data were analyzed by two-tailed unpaired t tests. See also Figure S7.

Since DAMPs such as histones can be toxic when they reach a high level *in vivo*,[38] the increase of DAMPs to a non-lethal level in TNF-treated mice might synergize with TNF to promote animal death. In this case, administering a non-lethal dose of histone could potentially substitute for the cecum damage in TNF-induced mouse death. Indeed, intravenous injection of a

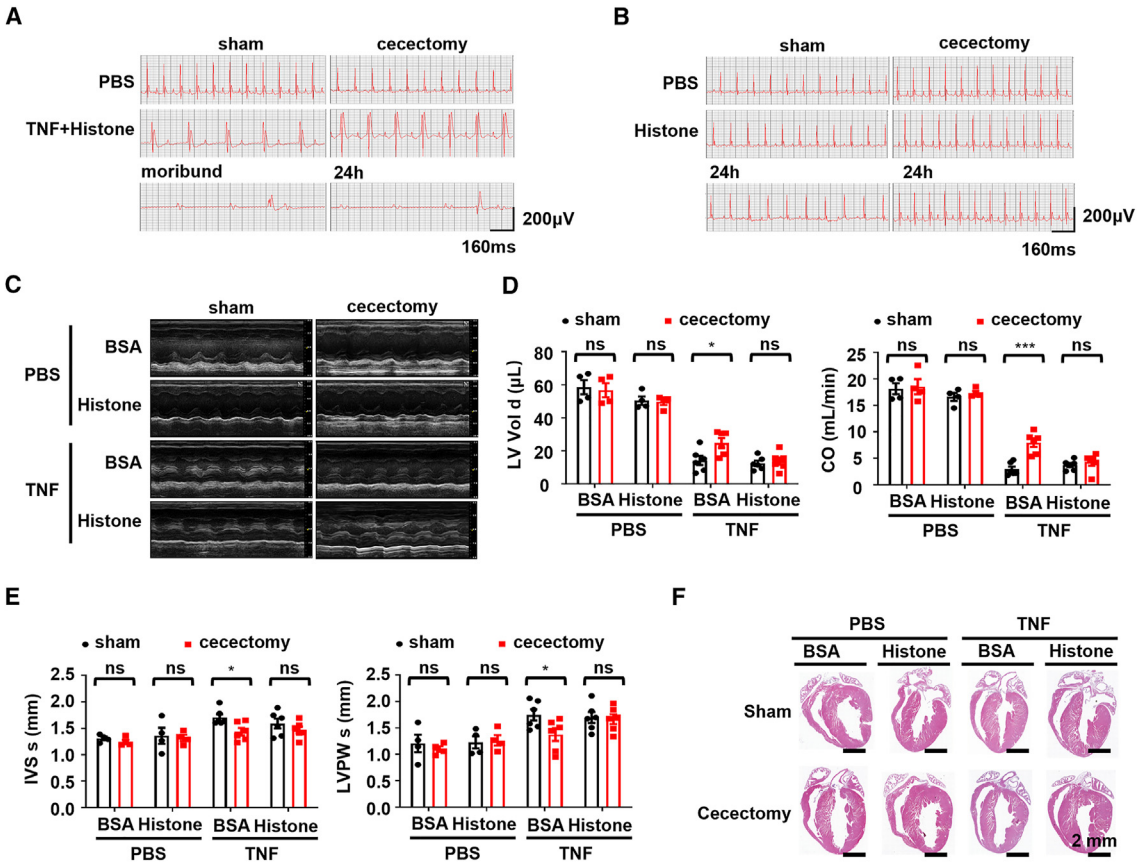

Figure 4. Histones can bypass cecectomy and synergize with TNF in promoting cardiac dysfunction

(A) ECG of TNF-treated cecectomized or sham wild-type mice injected with histones, recorded at 8 or 24 h (or when moribund).

(B) Same as (A) but with mice receiving histones only ($n = 6$).

(C–F) Cecectomized or sham mice treated with TNF and histones or BSA. Cardiac function was measured 8 h post-TNF ($n = 4$) (C). Shown are quantitative analysis of LV vol, d and CO (D), IVS, s, and LVPW, s (E), and representative H&E staining of the heart (F).

Cumulative results of two or three independent experiments are shown. Mean ± SEM is indicated by small horizontal lines. Each symbol represents a representative sample. The small horizontal lines indicate the means ± sems. ns, not significant, $P > 0.05$; *, $P < 0.05$; **, $P < 0.01$; ***, $P < 0.001$; ****, $P < 0.0001$. The data were analyzed by two-tailed unpaired *t* tests. See also Figure S7 and Video S2.

non-lethal dose of histone after TNF injection resulted in hypothermia and the death of mice that had undergone cecectomy (Figure 3E), while administration of the same concentration of BSA had no effect (Figures 3E and S7H). Supplementation of a non-lethal dose of histone to TNF-treated *Mlkl*$^{-/-}$ or *Rip3*$^{-/-}$ mice also triggered hypothermia and mouse death (Figures 3F and 3G). Thus, TNF-induced mouse death should result from the synergy of TNF and the DAMPs released by TNF-induced necroptosis of cecal cells.

Histones synergize with TNF to cause lethal cardiac dysfunction

Since necroptosis in the cecum is required for cardiac dysfunction in TNF-treated mice, we tested whether administering a non-lethal dose of histone affects cardiac function in TNF-treated mice. Histone administered after TNF injection caused similar cardiac dysfunction in both cecectomized and sham mice, whereas treatment with the same concentration of histones alone did not cause any significant cardiac dysfunction (Figures 4A and 4B). Moreover, histone administration decreased the LV volume and CO to similar extents in both TNF-treated sham mice and cecectomized mice, while the same concentration of histone alone had only slight effects on cardiac function (Figures 4C–4E; Video S2). No significant structural changes were observed in the hearts of TNF-treated mice, regardless of whether they were administered histones (Figure 4F). Similar results were obtained when *Mlkl*$^{-/-}$ mice and their wild-type littermates were used (Figures S7I–S7M). Thus, histones in the circulation can synergize with TNF to impair cardiac function. These findings suggest that DAMPs released from necroptotic cecal cells in TNF-treated mice synergize with TNF to impair cardiac function.

DAMPs act via various sensing/activation pathways to synergize with TNF in triggering mouse death

Since histone administration can restore the sensitivity of cecectomized, *Mlkl*$^{-/-}$, and *Rip3*$^{-/-}$ mice to TNF-induced mouse death, we explored how endogenously produced DAMPs function in TNF-treated mice. It is well known that Toll-like receptors

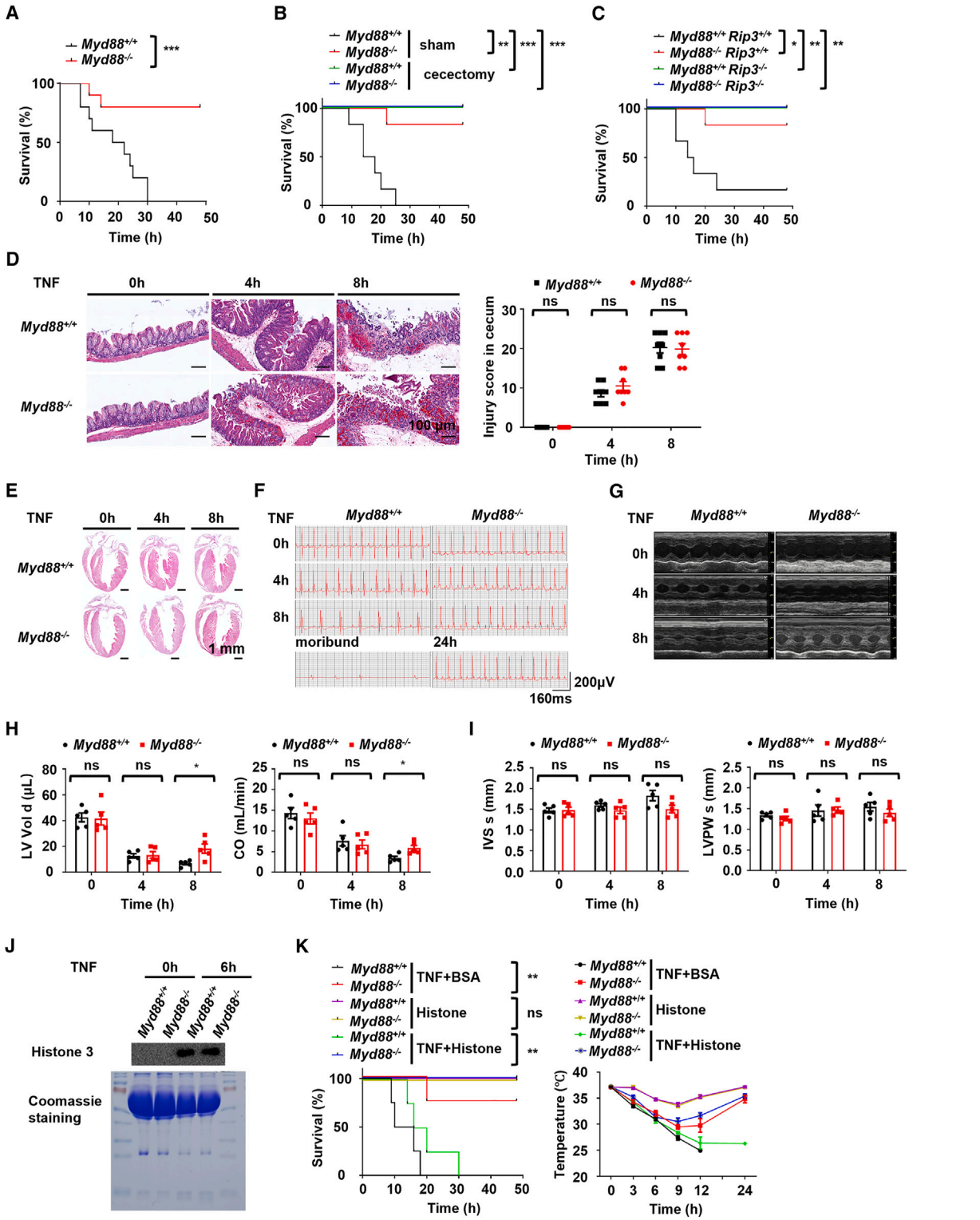

Figure 5. Cecal cell necroptosis-promoted lethal cardiac dysfunction is primarily mediated by Myd88

(A) Mortality rate of TNF-treated *Myd88*$^{-/-}$ mice and *Myd88*$^{+/+}$ mice (n = 10).

(B and C) Mortality rates in TNF-treated *Myd88*$^{-/-}$ with cecectomy or sham surgery (B) and *Myd88*$^{-/-}$*Rip3*$^{-/-}$ mice (C) and their wild-type littermates (n = 6).

(D) Histological analysis and scoring of cecal tissues from TNF-treated mice (n = 8).

(E) Histological changes in hearts of TNF-treated *Myd88*$^{-/-}$ mice and *Myd88*$^{+/+}$ mice.

(legend continued on next page)

(TLRs) recognize many DAMPs and pathogen-associated molecular patterns (PAMPs),[39] and reductions in TNF-induced death in *Tlr2*$^{-/-}$, *Tlr4*$^{-/-}$, and *Tlr9*$^{-/-}$ mice have been reported in some studies.[40,41] However, deletion of *Tlr2*, *Tlr4*, or *Tlr9* alone in mice did not significantly protect against TNF-induced death in our experiments (Figures S8A–S8C). This is not surprising, given that each of these receptors can sense only a few DAMPs.[39] We then generated *Tlr2*$^{-/-}$*Tlr4*$^{-/-}$ and *Tlr2*$^{-/-}$*Tlr4*$^{-/-}$*Tlr9*$^{-/-}$ mice. Although no significant differences in mouse survival were observed between knockout mice and their wild-type littermates, the mortality rate of the *Tlr2*$^{-/-}$ *Tlr4*$^{-/-}$ and *Tlr2*$^{-/-}$ *Tlr4*$^{-/-}$ *Tlr9*$^{-/-}$ mice tended to be decreased (Figures S8D and S8E). Since signaling through many DAMP receptors involves the adaptor protein Myd88, we then assessed the survival rate of TNF-treated *Myd88*$^{-/-}$ mice and found that their survival rate was significantly increased (Figure 5A). In contrast, deficiency of *Trif*, another important adaptor protein,[42] did not exert any protective effects against TNF-induced death (Figure S8F). Moreover, compared with *Myd88*$^{-/-}$ mice, *Myd88*$^{-/-}$*Trif*$^{-/-}$ mice did not exhibit additional protection against TNF-induced death (Figure S8G). Thus, the activation of various Myd88-dependent pathways participates in TNF-induced mouse death.

To further determine whether the DAMPs released from necroptotic cecal cells act via the Myd88 pathway to elicit a death-promoting effect, we compared TNF-induced mortality rates between *Myd88*$^{-/-}$ mice and their wild-type littermates after cecectomy or sham surgery. As shown in Figure 5B, compared with wild-type mice that had undergone cecectomy, no additional protective effect was observed in *Myd88*$^{-/-}$ mice that had undergone cecectomy. Moreover, we generated *Myd88*$^{-/-}$*Rip3*$^{-/-}$ mice and found that *Myd88* and *Rip3* deficiency had no additional effect in protecting against TNF-induced death (Figure 5C). Thus, Myd88 and cecal cell necroptosis are on the same axis in promoting mouse death.

Myd88 deficiency blocks TNF-induced cardiac dysfunction

Cardiac dysfunction occurs downstream of cecal cell necroptosis in TNF-treated mice. Thus, we aimed to determine how the Myd88-mediated cellular response contributes to the pathological changes induced by TNF treatment in mice. TNF injection induced rapid epithelial cell death and submucosal edema of comparable severity in the cecum of both wild-type and *Myd88*$^{-/-}$ mice (Figure 5D), and the release of major inflammatory lipid mediators and cytokines was almost comparable between wild-type and *Myd88*$^{-/-}$ mice (Figures S8I–S8U). These data indicate that Myd88 is not required for TNF-induced cecal epithelial damage or inflammatory responses.

When the heart was analyzed, we did not find significant differences in heart structure between TNF-treated *Myd88*$^{-/-}$ mice and their wild-type littermates (Figure 5E). However, significant differences in their ECG were observed (Figure 5F), and echocardiography revealed that the LV volume and CO were significantly bigger in *Myd88*$^{-/-}$ mice than in their wild-type littermates 8 h after TNF injection (Figures 5G–5I; Video S2), indicating that Myd88 signaling promotes cardiac dysfunction in TNF-treated mice. Consistent with the findings regarding cecal damage, the serum histone 3 concentration in TNF-treated *Myd88*$^{-/-}$ mice and their wild-type littermates was not significantly different (Figure 5J). Importantly, histone administration failed to restore the sensitivity of *Myd88*$^{-/-}$ mice to TNF, which was demonstrated by the fact that *Myd88*$^{-/-}$ mice still exhibited resistance to hypothermia and death after histone administration (Figures 5K and S8H). Thus, Myd88 mediates the histone-elicited cellular response, leading to the deterioration of cardiac function.

TNF and histones cooperate to affect cardiac function

To further verify whether TNF and histones directly influence cardiac function, Langendorff perfusion experiments were performed.[43] ECG of isolated hearts was performed with a 32-channel multi-electrical array, and TNF and/or histones were added to the perfusate to observe their effects on the heart (Figure 6A). TNF administration alone did not cause significant changes in perfused wild-type hearts even with a very high dose (Figures S9A–S9C), but when a low dose (5 μg/mL) of histones was added to the perfusate containing a low dose of TNF (0.3 μg/mL), a prolonged ECG interval, a widened QRS complex, and ST elevation were observed, and cardiac arrest occurred within 20 min, confirming that TNF and histones cooperate to cause cardiac dysfunction (Figures 6B and 6C). The addition of histones to the TNF-containing perfusate also caused severe cardiac dysfunction in perfused *Rip3*$^{-/-}$ mouse hearts but not perfused *Myd88*$^{-/-}$ mouse hearts, confirming that Myd88 signaling in the heart is required for TNF- and histone-induced cardiac dysfunction (Figures 6B and 6C).

We also analyzed the activity time recorded by each electrical array detector. Consistent with the ECG results, equal activity times were observed in the hearts of the wild-type, *Myd88*$^{-/-}$, and *Rip3*$^{-/-}$ mice when PBS was added to the perfusate, and TNF administration had no significant influence on the activity time (Figure 6D). However, the activity time recorded by several detectors was significantly increased in both wild-type and *Rip3*$^{-/-}$ mouse hearts after histone administration, and this change caused by histone administration was efficiently blocked by *Myd88* deficiency (Figure 6D). Similar changes in the

(F) ECG results of TNF-treated *Myd88*$^{-/-}$ mice and *Myd88*$^{+/+}$ mice at the indicated times.
(G–I) ECG results of TNF-treated *Myd88*$^{-/-}$ mice and *Myd88*$^{+/+}$ mice at the indicated times (G), LV vol, d and CO (H), and IVS, s and LVPW, s (I) were quantitatively analyzed (n = 5).
(J) Serum histone 3 levels in TNF-treated mice with total serum proteins as loading control.
(K) Mortality rate and rectal temperature of TNF-treated *Myd88*$^{-/-}$ mice and *Myd88*$^{+/+}$ mice (n = 4) injected with histones or BSA.
Scale bars: 100 μm (D) and 1 mm (E). Cumulative results from two or three independent experiments are shown. Mean ± SEM is indicated by small horizontal lines. Each symbol represents a representative sample. The survival curve is presented as a Kaplan-Meier plot. The small horizontal lines indicate the means ± sems. ns, not significant, $P > 0.05$; *, $P < 0.05$; **, $P < 0.01$; ***, $P < 0.001$; ****, $P < 0.0001$. The data were analyzed by two-tailed unpaired t tests. See also Figures S8 and Video S2.

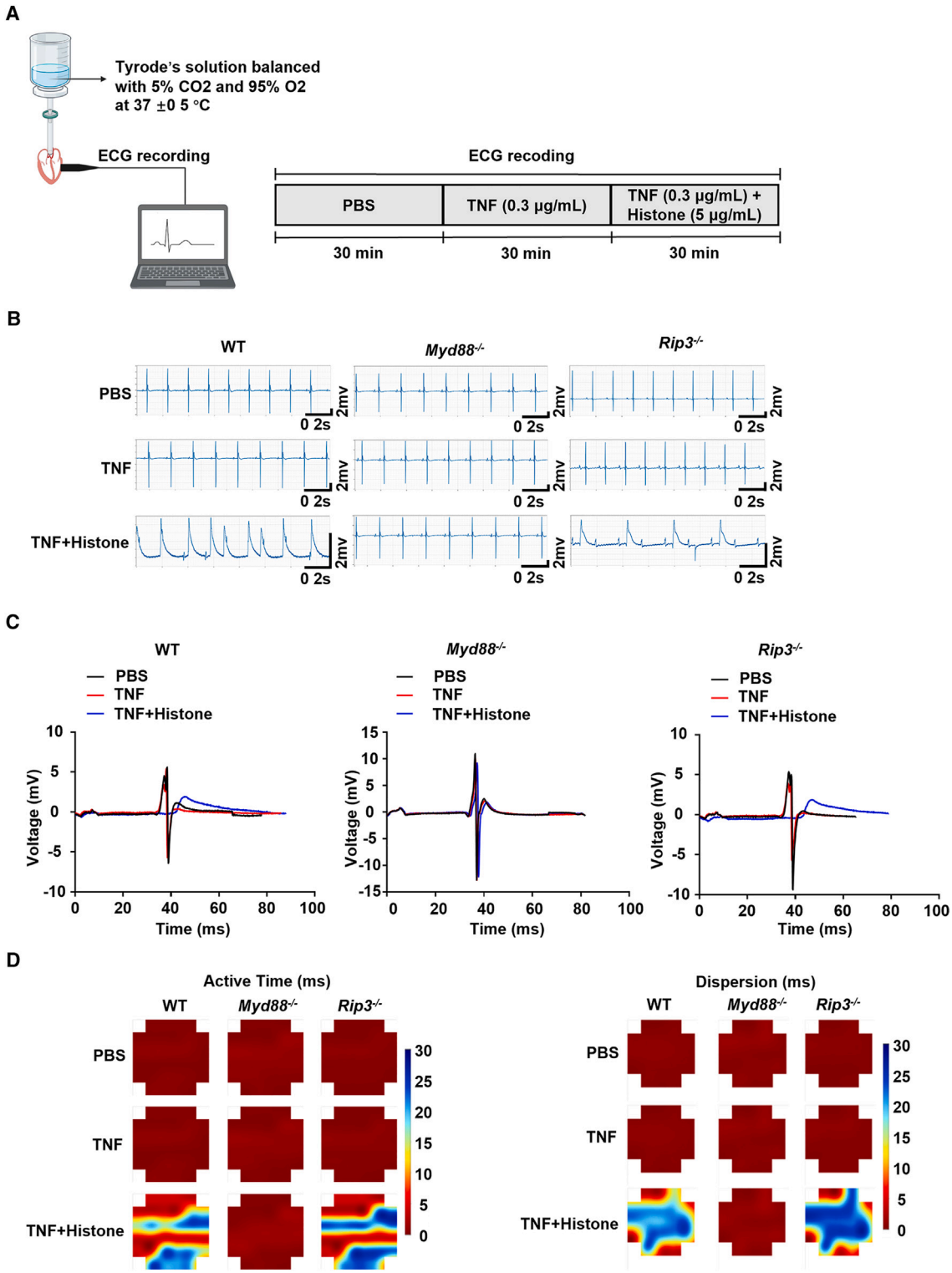

Figure 6. Myd88 is essential for the synergy of TNF and histones in inducing cardiac dysfunction *in vitro*

(A) Workflow of the *in vitro* Langendorff perfusion experiments.

(B–D) Representative examples of electrocardiogram tracings (B) and single electrocardiogram tracings (C) and the active time and dispersion time (D) of perfused wild-type, *Myd88*$^{-/-}$, and *Rip3*$^{-/-}$ mouse hearts.

Cumulative results from two or three independent experiments are shown. See also Figure S9.

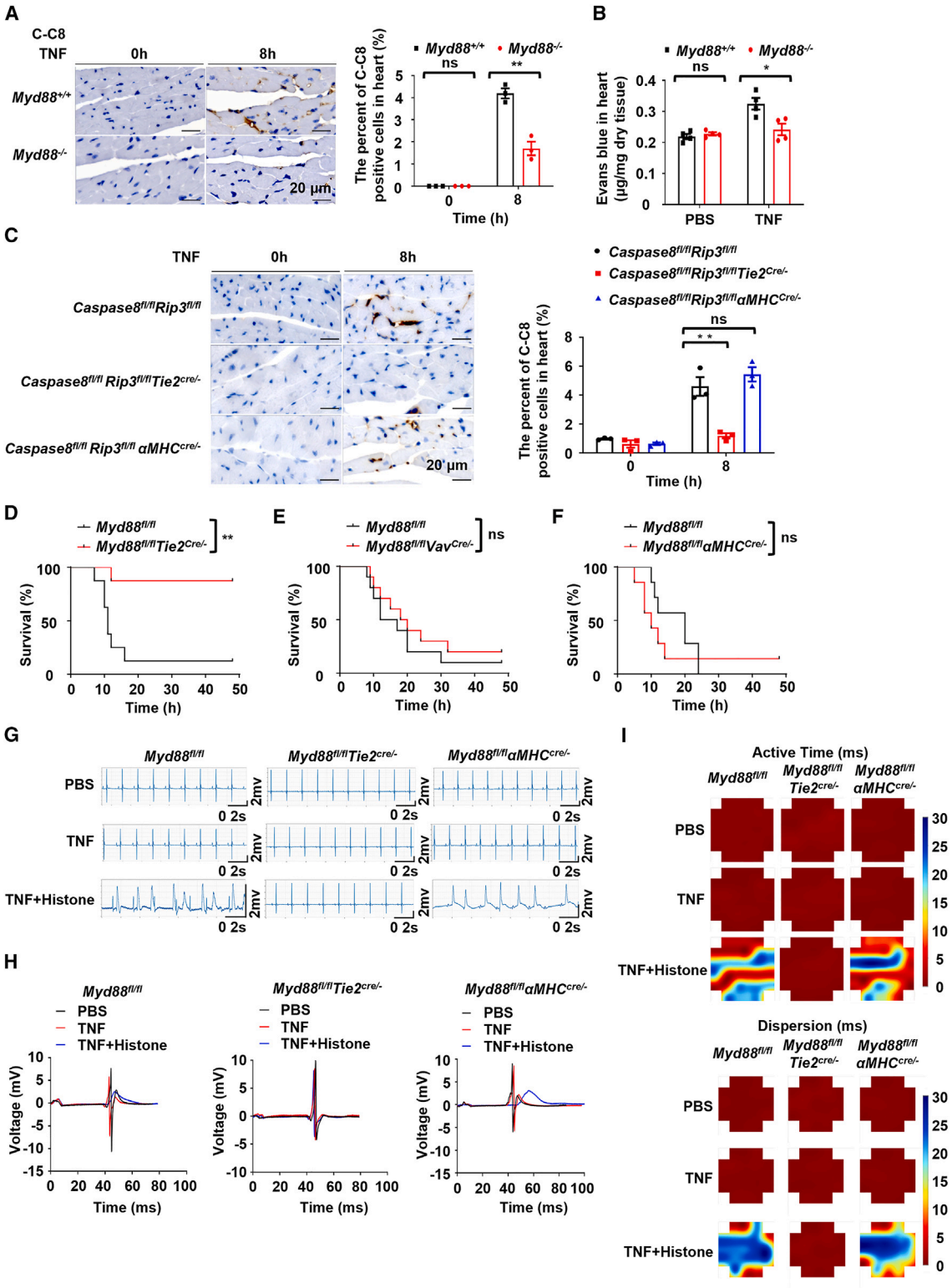

Figure 7. Myd88-caspase-8 axis in cardiac endothelial cells is essential for the lethal cardiac dysfunction in TNF-treated mice

(A) *Myd88*$^{-/-}$ mice and *Myd88*$^{+/+}$ mice were injected with TNF. Shown are cleaved caspase-8 (C-C8) signals in cardiac tissue from TNF-injected *Myd88*$^{-/-}$ mice and *Myd88*$^{+/+}$ mice.

(B) Cardiac vascular permeability in TNF-injected *Myd88*$^{-/-}$ mice and *Myd88*$^{+/+}$ mice assessed by Evans blue assay.

(legend continued on next page)

dispersion time were also observed, as a significantly increased dispersion time was recorded by most detectors in both wild-type and *Rip3*$^{-/-}$ mouse hearts after histone administration but not in *Myd88*$^{-/-}$ mouse hearts (Figure 6D). Moreover, the addition of the same concentration of histones alone to the perfusate did not cause significant changes in the ECG results in wild-type, *Myd88*$^{-/-}$, or *Rip3*$^{-/-}$ mouse hearts (Figures S9D and S9E), and the activation time and dispersion time were also comparable between wild-type, *Myd88*$^{-/-}$, and *Rip3*$^{-/-}$ mouse hearts (Figure S9F). Collectively, these results suggest that the heart is a direct target of TNF and histones, consistent with the findings obtained in mice injected with TNF or TNF and histones (Figures 2, 3, and 4).

Myd88-dependent DAMP signaling in cardiac endothelial cells occurs via caspase-8 to synergize with TNF signaling in inducing cardiac dysfunction

Although not as primary as the necroptotic pathway in mediating TNF-induced mouse death, the apoptotic (caspase-8) pathway coordinates with the necroptotic pathway to promote *in vivo* toxicity of TNF.[9] At LD_{100}, TNF-induced mouse death is primarily mediated by the cecum-heart axis, while higher TNF doses can induce cell death in other organs that may also initiate mouse death. Simultaneous deletion of *Casp8* and *Rip3* blocks TNF-induced mouse death,[9] even with doses up to 5 times LD_{100} (Figure S10A). ECG waveforms, echocardiography data, LV volume, and CO were similar between TNF-treated *Casp8*$^{-/-}$*Rip3*$^{-/-}$ mice and untreated *Casp8*$^{-/-}$*Rip3*$^{-/-}$ mice (Figures S10B–S10E), and hearts from these mice were resistant to TNF- and histone-induced cardiac dysfunction in *ex vivo* Langendorff perfusion experiments (Figures S10F–S10K). No or very slight damage was observed in the cecum of TNF-treated *Casp8*$^{-/-}$*Rip3*$^{-/-}$ mice (Figure S10L). These findings indicate that deletion of both *Casp8*$^{-/-}$ and *Rip3*$^{-/-}$ blocks all damage in both the executor and initiator organs.

Caspase-8 activation can be measured with an antibody specific for caspase-8 cleaved at D374 (C-C8), and necroptotic pathway activation can be detected with an anti-p-MLKL antibody.[44] We examined cardiac C-C8 and p-MLKL levels in TNF-treated *Myd88*$^{-/-}$ mice and their wild-type littermates. C-C8 signals were observed in wild-type mouse cardiac tissues; most of these signals appeared to be in endothelial cells, and the C-C8 signals were barely detectable in *Myd88*$^{-/-}$ mouse cardiac tissues (Figure 7A), suggesting that caspase-8 activation is downstream of Myd88. Indeed, Myd88-dependent caspase-8 activity has been observed in some pathological processes.[45–47] In contrast, we did not detect p-MLKL signals in the hearts of TNF-treated wild-type or *Myd88*$^{-/-}$ mice (Figure S10M). The damage of cardiac endothelial cells was supported by the increase of cardiac vascular permeability to Evans blue in TNF-treated wild-type mice but much less severe in *Myd88*$^{-/-}$ mice (Figure 7B).

Since Myd88-dependent C-C8 signals, but not p-MLKL signals, were detected most likely in cardiac endothelial cells (Figures 7A and S10M), and the *Rip3*$^{-/-}$ mouse heart responded similarly to TNF and histones as the wild-type mouse heart in the Langendorff perfusion experiment (Figures 6B–6D), caspase-8 rather than RIP3/MLKL is likely downstream of Myd88 to mediate the cardiac dysfunction. To verify the pathological role of caspase-8, *Caspase8*$^{fl/fl}$*Rip3*$^{fl/fl}$*Tie2*$^{Cre/-}$ (endothelial cell-specific knockout) mice and *Caspase8*$^{fl/fl}$*Rip3*$^{fl/fl}$$\alpha$*MHC*$^{Cre/-}$ (cardiomyocyte-specific knockout) mice were generated. As shown in Figure 7C, obvious and comparable C-C8 signals were observed in cardiac tissues from TNF-treated *Caspase8*$^{fl/fl}$*Rip3*$^{fl/fl}$ mice and *Caspase8*$^{fl/fl}$*Rip3*$^{fl/fl}$$\alpha$*MHC*$^{Cre/-}$ mice but barely observed in *Caspase8*$^{fl/fl}$*Rip3*$^{fl/fl}$*Tie2*$^{Cre/-}$ mice. These data supported the role of caspase-8 in cardiac endothelial cells. Consistent with this, TNF and histones impaired cardiac function to a similar extent in *Caspase8*$^{fl/fl}$*Rip3*$^{fl/fl}$ mouse hearts and *Caspase8*$^{fl/fl}$*Rip3*$^{fl/fl}$$\alpha$*MHC*$^{Cre/-}$ mouse hearts in the Langendorff perfusion experiment, but *Caspase8*$^{fl/fl}$*Rip3*$^{fl/fl}$*Tie2*$^{Cre/-}$ mouse hearts showed resistance (Figures S11A–S11C). The same dose of histones alone did not cause any ECG changes (Figures S11D–S11F). Since *Tie2*$^{Cre/-}$ mice have been reported to have leakage of hematopoietic stem cells,[48] we also generated *Caspase8*$^{fl/fl}$*Rip3*$^{fl/fl}$*Vav*$^{Cre/-}$ mice and found that the response of the *Caspase8*$^{fl/fl}$*Rip3*$^{fl/fl}$*Vav*$^{Cre/-}$ mouse heart to TNF and histones was similar to that of the wild-type mouse heart in the Langendorff perfusion experiment (Figure S11). Thus, caspase-8 activity downstream of Myd88 in cardiac endothelial cells appears to play a key role in cardiac dysfunction of TNF-treated mice.

To confirm that cardiac endothelial cells are the major targeting cells of DAMPs in TNF-induced mouse death, we generated *Myd88*$^{fl/fl}$*Tie2*$^{cre/-}$ mice and found that these mice were indeed protected from TNF-induced death (Figure 7D). In contrast, the mortality rates of *Myd88*$^{fl/fl}$*Vav*$^{cre/-}$ mice (Figure 7E) and *Myd88*$^{fl/fl}$$\alpha$*MHC*$^{Cre/-}$ mice (Figure 7F) were comparable to those of their wild-type littermates after TNF treatment. Langendorff perfusion experiments revealed that, opposite to *Myd88* $^{fl/fl}$ and *Myd88*$^{fl/fl}$$\alpha$*MHC*$^{Cre/-}$ mouse hearts, *Myd88*$^{fl/fl}$*Tie2*$^{cre/-}$ mouse hearts were resistant to TNF and histone-induced severe cardiac dysfunction (Figures 7G–7I), while the same dose of histones alone did not cause any cardiac dysfunction (Figures S12A–S12C). Thus, Myd88 functions in cardiac endothelial cells to promote TNF-induced lethal cardiac dysfunction and mouse death. Collectively, we can summarize

(C) Immunohistochemical staining for C-C8 in heart sections from TNF-injected *Caspase8*$^{fl/fl}$*Rip3*$^{fl/fl}$, *Caspase8*$^{fl/fl}$*Rip3*$^{fl/fl}$*Tie2*$^{cre/-}$, and *Caspase8*$^{fl/fl}$*Rip3* $^{fl/fl}$$\alpha$*MHC*$^{cre/-}$ mice (n = 6).

(D–F) Mortality rates in TNF-injected *Myd88*$^{fl/fl}$*Tie2*$^{cre/-}$ (D, n = 8), *Myd88*$^{fl/fl}$*Vav*$^{cre/-}$ (E, n = 10), and *Myd88*$^{fl/fl}$$\alpha$*MHC*$^{cre/-}$ (F, n = 7) mice and their wild-type littermates.

(G–I) ECG results from Langendorff perfusion experiments: representative traces (G), single ECG tracings (H), and active and dispersion times (I) in *Myd88* $^{fl/fl}$, *Myd88*$^{fl/fl}$*Tie2*$^{cre/-}$ and *Myd88*$^{fl/fl}$$\alpha$*MHC*$^{cre/-}$ mouse hearts.

Scale bars: 20 μm (A and C). Cumulative results from two or three independent experiments are shown. Each symbol represents a representative sample. The survival curve is presented as a Kaplan-Meier plot. The small horizontal lines indicate the means ± sems. ns, not significant, $P > 0.05$; *, $P < 0.05$; **, $P < 0.01$; ***, $P < 0.001$; ****, $P < 0.0001$. The data were analyzed by two-tailed unpaired t tests. See also Figures S10–S12.

the signaling course of TNF-induced mouse death as follows: TNF induces necroptosis of cecal IECs, and the DAMPs released from necroptotic cecum synergize with TNF, leading to injury of cardiac endothelium, which causes lethal cardiac dysfunction and mouse death, and the Myd88-caspase-8 axis mediates the effects in cardiac endothelial cells.

DISCUSSION

Animal models using TNF superfamily members, such as TNF and FasL, have provided valuable insights into the mechanisms underlying mouse death mediated by intrinsic mediators.[2,49] Fas ligation results in rapid and severe liver damage, but its connection to systemic collapse has not been explored experimentally, although hemorrhage has been proposed as a possible cause of lethality.[50] TNF is known to induce SIRS, and it has been commonly assumed that excessive SIRS leads to animal death. However, the findings that TNF-induced necroptosis initiates TNF-triggered mouse death[11] and that *Rip3*$^{fl/fl}$*Villin*$^{cre/-}$ mice[9] or IEC-specific *Tnfr1* knockout mice[51] are resistant to TNF-induced death suggest the linkage of necroptosis-mediated organ damage and TNF-induced lethality. Cecum injury was observed in a very early study of TNF,[2] and our previous research showed that the cecum damage is primarily due to RIP3-dependent necroptosis,[10] a finding supported by multiple other studies.[52–56] Our cecectomy experiments unequivocally demonstrate that cecal cell necroptosis initiates TNF-induced mouse death (Figure 1). Furthermore, we show that DAMPs released from necroptotic cecal cells synergize with TNF to induce lethal cardiac failure (Figures 3, 4, and S7H–S7M), indicating a sequential organ failure process in TNF-induced mouse death, where specific organs act as initiators and executors of the lethal process.

The sensitivity of the cecum to TNF-induced necroptosis *in vivo* may be attributed to its unique histological structure or extracellular environment, potentially involving exposure to chyme or aerobic bacteria. The detection of cecal epithelial cell death does not exclude the possibility of other forms of cell death occurring at levels too low to be detected. The contribution of the death of other cells is possible, since cecectomy only mildly restored LV volume and CO in TNF-treated mice, but almost complete restoration can be observed in *Caspase8* and *Rip3* double-knockout mice (Figures 2 and S10). Another consideration is that cecal epithelial cells may die too quickly for detection when using short-term LD_{100} TNF treatment. This may not be the case, as no IEC death, apart from cecal cells, was detected, even with prolonged LD_{50} TNF treatment. Instead, TNF with a dose much higher than LD_{100} can cause quick damage in intestines in addition to cecal epithelia in both wild-type and cecectomized mice. The lethal DAMPs need not be solely released by the cecum to accelerate animal death, as higher TNF levels can induce cell death in other parts of the intestines, which could also serve as major sources of DAMPs. Under these conditions, injury to other parts of the intestines could also act as initiators of acute animal death. DAMPs appear to be more crucial in interfering with cardiac function, since high-dose TNF alone did not significantly impact perfused hearts *ex vivo* (Figures S9A–S9C). Given that endothelial cells are sensitive to both TNF and DAMPs and that *Tnfr1* deficiency on cardiomyocytes had no effect in *in vitro* Langendorff perfusion experiments (Figures S12D-S12F), TNF and DAMPs likely synergize on endothelial cells rather than on cardiomyocytes directly. Our ECG and echocardiography analyses demonstrate bradycardia, myocardial ischemia, and a progressive reduction in CO in TNF-treated mice (Figures 2A–2D). Interestingly, both cecectomy and the genetic deletion of *Rip3* or *Mlkl* in mice improved cardiac function (Figures 2A–2D and S5A–S5H). Atropine was found to effectively enhance mouse survival by rescuing cardiac function (Figures 2E–2J), demonstrating that cardiac dysfunction is the primary cause of mouse death. By using histones to mimic the effect of DAMPs, we confirmed the synergistic effect of TNF and TNF-induced DAMPs in triggering lethal cardiac dysfunction *in vivo* (Figures 3E–3G, 4, and S7H–S7M) and *ex vivo* (Figure 6). Furthermore, histone administration bypassed the requirement for cecal cell necroptosis in inducing death in TNF-treated mice. DAMPs are recognized by various receptors, with Myd88 acting as a common adaptor (Figures 5A–5D and S8A–S8H). Using cell-type-specific deletion of *Myd88* or *Casp8* in mice, we demonstrated that the lethal effect of DAMPs occurs via the Myd88-caspase-8 axis. Given that caspase-8 is a downstream effector of TNF signaling, the primary cause of TNF-induced mouse death likely involves the synergistic effect of TNF and DAMPs via caspase-8, leading to damage in cardiac endothelial cells (Figure 7).

It is noteworthy that some pathological changes in the hearts of TNF-treated mice differ from those observed in LPS- or cecal ligation puncture (CLP)-treated mice. Unlike the CLP model, which shows early diastolic dysfunction followed by late-stage cardiomyocyte damage, immune cell infiltration, and systolic dysfunction,[24,35,57,58] TNF-treated mice exhibited slight cardiomyocyte damage without immune cell infiltration (Figures 4 and S6). Consistently, necroptosis elimination did not protect against LPS- or CLP-induced mouse death.[13] TNF-induced mouse death may thus serve as a model for studying the continuous deterioration of diastolic function *in vivo*.

It is known that administration of sufficient histones alone can cause rapid mouse death, likely due to physical/chemical damage to lung epithelia.[38,59] Non-lethal doses of histones activate innate immune responses via TLRs.[40,59] Other DAMPs besides histones likely play a role in TNF-induced death, as the combined deletion of *Tlr2*, *Tlr4*, and *Tlr9* had an additive protective effect (Figures S8A–S8E). We detected TNF-induced serum release of HMGB1, a well-known DAMP, by ELISA, but blocking HMGB1 by genetic deletion, neutralizing antibody or *Rage* (a major receptor for HMGB1) deficiency failed to prevent TNF-induced lethality at LD_{100}. HMGB1 may still participate in the TNF-induced process of mouse death but be dispensable for mouse death. Endothelial cell necroptosis-induced vascular hyperpermeability and coagulation in the liver have been proposed as major contributors to TNF-induced death in *Rip1* kinase-dead mutant mice (*Rip1*$^{D138N/D138N}$ mice).[8] Although we observed liver vascular hyperpermeability and endothelial coagulation in TNF-treated mice, these changes were comparable between wild-type mice and death-resistant mice (cecectomized, *Rip3*$^{-/-}$ or *Mlkl*$^{-/-}$ mice) (Figure S4), suggesting that liver changes may not be the primary cause of TNF-induced mouse death under our experimental conditions.

The transduction of DAMP signals by circulating extracellular histones to distal organs has been observed in several studies.[60,61] Non-microbial factors in the intestinal mesenteric lymph after hemorrhagic shock have been reported to recreate lung injury via TLR4 activation, with many of these toxic gut-derived factors identified as DAMPs, such as histones.[38,59,62] Our study demonstrates that DAMPs serve as signal molecules for inter-organ communication in TNF-induced mouse death. The strength of the synergy between TNF and DAMPs, along with their impact on vital organs, determines the survival or death of TNF-treated mice.

Our findings shed light on the role of inter-organ communication in driving TNF-induced mortality in mice, revealing a strong correlation between circulating DAMPs (especially histones) and cardiac dysfunction and mortality in clinically septic or critically ill patients.[18,63] It also provides valuable insights into the mechanisms of inflammatory disorders and potentially guide the development of targeted therapies.

Limitations of the study

Since the aim of this study is the pathological process of TNF-induced animal death, we used an LD_{100} dose of TNF to ensure that all mice analyzed were undergoing the process of death. However, we shall mention that a lower dose of TNF, such as an LD_{50} dose, may result in a slower dying process, which could differ from the quick death induced by LD_{100} TNF. This study also has not addressed the potential role of cecum necroptosis in non-lethal dose TNF-challenged mice. It has been reported that neutralization of histone benefits severe SIRS.[38] Currently, we lack an effective method to evaluate the contribution of the other DAMPs to TNF-induced lethality. TNF has been reported to induce necroptosis of epithelial cells in other parts of the intestine.[11,16,38] At present, we do not know whether the published study overlooked the cecum or whether the cecum was not more sensitive to TNF-induced necroptosis. There could be variations among different studies from different laboratories. Moreover, numerous DAMPs have been identified across various levels of disease progression[64,65]; their interactions with PAMPs are not addressed in this study.

RESOURCE AVAILABILITY

Lead contact

Requests for further information, resources, and reagents should be directed to and will be fulfilled by the lead contact, Jiahuai Han (jhan@xmu.edu.cn).

Materials availability

This study did not generate new unique reagents.

Data and code availability

- The serum mass spectrometry data generated in this study have been deposited in the Integrated Proteome Resources Database under accession code PXD048104 (https://proteomecentral.proteomexchange.org/cgi/GetDataset?ID=PXD048104). The *Mus musculus* proteome used for MS analysis was downloaded from UniProt.
- This study did not report original code.
- Any additional information required to reanalyze the data reported in this work paper is available from the lead contact upon request.

ACKNOWLEDGMENTS

The authors thank Prof. Jie Du and Prof. Yulin Li for cardiac tissue histopathology, Prof. Chuanqi Zhong for serum mass spectrometry, Prof. Kairui Mao for immunohistochemistry, and Prof. Yibin Wang for manuscript suggestions. The graphical abstract was created using BioRender. This work was supported by the National Natural Science Foundation of China (82388201 to J.H.), the National Key R&D Program of China (2020YFA0803500 to J.H. and 2020YFA0803501 to J.W.), the National Natural Science Foundation of China (32470944 to J.W. and 32100736 to P.H.), the CAMS Innovation Fund for Medical Sciences (2019-I2M-5-062 to J.H.), the Fujian Province Central to Local Science and Technology Development Special Program (2022L3079 to J.H.), the Fu-Xia-Quan Zi-Chuang District Cooperation Program (3502ZCQXT2022003 to J.H.), the Xiamen Natural Science Foundation Project (3502Z202373004 to J.W.), and the China Postdoctoral Science Foundation (2021M691884 to P.H.).

AUTHOR CONTRIBUTIONS

J.W., T.A., P.H., Y.L., Q.S., M.C., and Z.Z. performed most of the experiments. J.W., T.A., P.H., W.C., and J.H. conceptualized and designed the project, interpreted the results, and prepared the manuscript. S.W. generated the transgenic mice and assisted in the breeding of related mice. J.W., T.A., and J.H. wrote the manuscript with contributions from all authors. J.W., T.A., and J.H. contributed to the data interpretation and discussions. W.J. and J.H. conceived and supervised the study.

DECLARATION OF INTERESTS

The authors declare no competing interests.

STAR★METHODS

Detailed methods are provided in the online version of this paper and include the following:

- KEY RESOURCES TABLE
- EXPERIMENTAL MODEL AND STUDY PARTICIPANT DETAILS
  - Mice
- METHOD DETAILS
  - TNF-induced SIRS
  - LPS-induced sepsis
  - Cecectomy
  - Detection of bacteria in blood
  - Collection of serum
  - ELISA
  - Histopathology
  - Wheat germ agglutinin (WGA) staining
  - Western blotting
  - Electrocardiography (ECG)
  - Echocardiography
  - Cardiac electrolyte and ATP analysis
  - Eicosanoid level analysis
  - Protein digestion and iTRAQ labeling
  - TimsTOF Pro mass spectrometry
  - Langendorff perfusion experiments
  - Vascular permeability assay
- QUANTIFICATION AND STATISTICAL ANALYSIS

SUPPLEMENTAL INFORMATION

Supplemental information can be found online at https://doi.org/10.1016/j.celrep.2024.114778.

Received: March 11, 2024
Revised: July 25, 2024
Accepted: September 4, 2024

REFERENCES

1. van Loo, G., and Bertrand, M.J.M. (2023). Death by TNF: a road to inflammation. Nat. Rev. Immunol. *23*, 289–303. https://doi.org/10.1038/s41577-022-00792-3.
2. Tracey, K.J., Beutler, B., Lowry, S.F., Merryweather, J., Wolpe, S., Milsark, I.W., Hariri, R.J., Fahey, T.J., 3rd, Zentella, A., Albert, J.D., et al. (1986). Shock and tissue injury induced by recombinant human cachectin. Science *234*, 470–474. https://doi.org/10.1126/science.3764421.
3. Bone, R.C. (1992). Toward an epidemiology and natural history of SIRS (systemic inflammatory response syndrome). JAMA *268*, 3452–3455.
4. Libert, C., Vink, A., Coulie, P., Brouckaert, P., Everaerdt, B., Van Snick, J., and Fiers, W. (1992). Limited involvement of interleukin-6 in the pathogenesis of lethal septic shock as revealed by the effect of monoclonal antibodies against interleukin-6 or its receptor in various murine models. Eur. J. Immunol. *22*, 2625–2630. https://doi.org/10.1002/eji.1830221023.
5. Everaerdt, B., Brouckaert, P., and Fiers, W. (1994). Recombinant IL-1 receptor antagonist protects against TNF-induced lethality in mice. J. Immunol. *152*, 5041–5049.
6. Takahashi, N., Vanlaere, I., de Rycke, R., Cauwels, A., Joosten, L.A.B., Lubberts, E., van den Berg, W.B., and Libert, C. (2008). IL-17 produced by Paneth cells drives TNF-induced shock. J. Exp. Med. *205*, 1755–1761. https://doi.org/10.1084/jem.20080588.
7. Huys, L., Van Hauwermeiren, F., Dejager, L., Dejonckheere, E., Lienenklaus, S., Weiss, S., Leclercq, G., and Libert, C. (2009). Type I interferon drives tumor necrosis factor-induced lethal shock. J. Exp. Med. *206*, 1873–1882. https://doi.org/10.1084/jem.20090213.
8. Zelic, M., Roderick, J.E., O'Donnell, J.A., Lehman, J., Lim, S.E., Janardhan, H.P., Trivedi, C.M., Pasparakis, M., and Kelliher, M.A. (2018). RIP kinase 1-dependent endothelial necroptosis underlies systemic inflammatory response syndrome. J. Clin. Invest. *128*, 2064–2075. https://doi.org/10.1172/JCI96147.
9. Newton, K., Dugger, D.L., Maltzman, A., Greve, J.M., Hedehus, M., Martin-McNulty, B., Carano, R.A.D., Cao, T.C., van Bruggen, N., Bernstein, L., et al. (2016). RIPK3 deficiency or catalytically inactive RIPK1 provides greater benefit than MLKL deficiency in mouse models of inflammation and tissue injury. Cell Death Differ. *23*, 1565–1576. https://doi.org/10.1038/cdd.2016.46.
10. Chen, W., Wu, J., Li, L., Zhang, Z., Ren, J., Liang, Y., Chen, F., Yang, C., Zhou, Z., Su, S.S., et al. (2015). Ppm1b negatively regulates necroptosis through dephosphorylating Rip3. Nat. Cell Biol. *17*, 434–444. https://doi.org/10.1038/ncb3120.
11. Duprez, L., Takahashi, N., Van Hauwermeiren, F., Vandendriessche, B., Goossens, V., Vanden Berghe, T., Declercq, W., Libert, C., Cauwels, A., and Vandenabeele, P. (2011). RIP kinase-dependent necrosis drives lethal systemic inflammatory response syndrome. Immunity *35*, 908–918. https://doi.org/10.1016/j.immuni.2011.09.020.
12. Polykratis, A., Hermance, N., Zelic, M., Roderick, J., Kim, C., Van, T.M., Lee, T.H., Chan, F.K.M., Pasparakis, M., and Kelliher, M.A. (2014). Cutting edge: RIPK1 Kinase inactive mice are viable and protected from TNF-induced necroptosis in vivo. J. Immunol. *193*, 1539–1543. https://doi.org/10.4049/jimmunol.1400590.
13. Wu, J., Huang, Z., Ren, J., Zhang, Z., He, P., Li, Y., Ma, J., Chen, W., Zhang, Y., Zhou, X., et al. (2013). Mlkl knockout mice demonstrate the indispensable role of Mlkl in necroptosis. Cell Res. *23*, 994–1006. https://doi.org/10.1038/cr.2013.91.
14. Takahashi, N., Duprez, L., Grootjans, S., Cauwels, A., Nerinckx, W., DuHadaway, J.B., Goossens, V., Roelandt, R., Van Hauwermeiren, F., Libert, C., et al. (2012). Necrostatin-1 analogues: critical issues on the specificity, activity and in vivo use in experimental disease models. Cell Death Dis. *3*, e437. https://doi.org/10.1038/cddis.2012.176.
15. Cauwels, A., Janssen, B., Waeytens, A., Cuvelier, C., and Brouckaert, P. (2003). Caspase inhibition causes hyperacute tumor necrosis factor-induced shock via oxidative stress and phospholipase A2. Nat. Immunol. *4*, 387–393. https://doi.org/10.1038/ni914.
16. Kaczmarek, A., Vandenabeele, P., and Krysko, D.V. (2013). Necroptosis: the release of damage-associated molecular patterns and its physiological relevance. Immunity *38*, 209–223. https://doi.org/10.1016/j.immuni.2013.02.003.
17. Ekaney, M.L., Otto, G.P., Sossdorf, M., Sponholz, C., Boehringer, M., Loesche, W., Rittirsch, D., Wilharm, A., Kurzai, O., Bauer, M., and Claus, R.A. (2014). Impact of plasma histones in human sepsis and their contribution to cellular injury and inflammation. Crit. Care *18*, 543. https://doi.org/10.1186/s13054-014-0543-8.
18. Cheng, Z., Abrams, S.T., Alhamdi, Y., Toh, J., Yu, W., Wang, G., and Toh, C.H. (2019). Circulating Histones Are Major Mediators of Multiple Organ Dysfunction Syndrome in Acute Critical Illnesses. Crit. Care Med. *47*, e677–e684. https://doi.org/10.1097/CCM.0000000000003839.
19. Denning, N.L., Aziz, M., Gurien, S.D., and Wang, P. (2019). DAMPs and NETs in Sepsis. Front. Immunol. *10*, 2536. https://doi.org/10.3389/fimmu.2019.02536.
20. Li, Y., Wan, D., Luo, X., Song, T., Wang, Y., Yu, Q., Jiang, L., Liao, R., Zhao, W., and Su, B. (2021). Circulating Histones in Sepsis: Potential Outcome Predictors and Therapeutic Targets. Front. Immunol. *12*, 650184. https://doi.org/10.3389/fimmu.2021.650184.
21. Van Hauwermeiren, F., Vandenbroucke, R.E., Grine, L., Lodens, S., Van Wonterghem, E., De Rycke, R., De Geest, N., Hassan, B., and Libert, C. (2015). TNFR1-induced lethal inflammation is mediated by goblet and Paneth cell dysfunction. Mucosal Immunol. *8*, 828–840. https://doi.org/10.1038/mi.2014.112.
22. Tuchschmidt, J., Fried, J., Astiz, M., and Rackow, E. (1992). Elevation of cardiac output and oxygen delivery improves outcome in septic shock. Chest *102*, 216–220. https://doi.org/10.1378/chest.102.1.216.
23. Mendoza, D.D., Cooper, H.A., and Panza, J.A. (2007). Cardiac power output predicts mortality across a broad spectrum of patients with acute cardiac disease. Am. Heart J. *153*, 366–370. https://doi.org/10.1016/j.ahj.2006.11.014.
24. Habimana, R., Choi, I., Cho, H.J., Kim, D., Lee, K., and Jeong, I. (2020). Sepsis-induced cardiac dysfunction: a review of pathophysiology. Acute Crit. Care *35*, 57–66. https://doi.org/10.4266/acc.2020.00248.
25. Krown, K.A., Page, M.T., Nguyen, C., Zechner, D., Gutierrez, V., Comstock, K.L., Glembotski, C.C., Quintana, P.J., and Sabbadini, R.A. (1996). Tumor necrosis factor alpha-induced apoptosis in cardiac myocytes. Involvement of the sphingolipid signaling cascade in cardiac cell death. J. Clin. Invest. *98*, 2854–2865. https://doi.org/10.1172/JCI119114.
26. Dhingra, S., Sharma, A.K., Arora, R.C., Slezak, J., and Singal, P.K. (2009). IL-10 attenuates TNF-alpha-induced NF kappaB pathway activation and cardiomyocyte apoptosis. Cardiovasc. Res. *82*, 59–66. https://doi.org/10.1093/cvr/cvp040.
27. Dhingra, S., Sharma, A.K., Singla, D.K., and Singal, P.K. (2007). p38 and ERK1/2 MAPKs mediate the interplay of TNF-alpha and IL-10 in regulating oxidative stress and cardiac myocyte apoptosis. Am. J. Physiol. Heart Circ. Physiol. *293*, H3524–H3531. https://doi.org/10.1152/ajpheart.00919.2007.
28. Kubota, T., McTiernan, C.F., Frye, C.S., Slawson, S.E., Lemster, B.H., Koretsky, A.P., Demetris, A.J., and Feldman, A.M. (1997). Dilated cardiomyopathy in transgenic mice with cardiac-specific overexpression of tumor necrosis factor-alpha. Circ. Res. *81*, 627–635. https://doi.org/10.1161/01.res.81.4.627.
29. Sun, L., Wang, H., Wang, Z., He, S., Chen, S., Liao, D., Wang, L., Yan, J., Liu, W., Lei, X., and Wang, X. (2012). Mixed lineage kinase domain-like protein mediates necrosis signaling downstream of RIP3 kinase. Cell *148*, 213–227. https://doi.org/10.1016/j.cell.2011.11.031.
30. Jongwattanapisan, P., Suntornsaratoon, P., Wongdee, K., Dorkkam, N., Krishnamra, N., and Charoenphandhu, N. (2012). Impaired body calcium metabolism with low bone density and compensatory colonic calcium

absorption in cecectomized rats. Am. J. Physiol. Endocrinol. Metab. *302*, E852–E863. https://doi.org/10.1152/ajpendo.00503.2011.

31. Kumari, P., Russo, A.J., Wright, S.S., Muthupalani, S., and Rathinam, V.A. (2021). Hierarchical cell-type-specific functions of caspase-11 in LPS shock and antibacterial host defense. Cell Rep. *35*, 109012. https://doi.org/10.1016/j.celrep.2021.109012.
32. Gao, H., Yang, T., Chen, X., and Song, Y. (2021). Changes of Lipopolysaccharide-Induced Acute Kidney and Liver Injuries in Rats Based on Metabolomics Analysis. J. Inflamm. Res. *14*, 1807–1825. https://doi.org/10.2147/JIR.S306789.
33. Vanden Berghe, T., Demon, D., Bogaert, P., Vandendriessche, B., Goethals, A., Depuydt, B., Vuylsteke, M., Roelandt, R., Van Wonterghem, E., Vandenbroecke, J., et al. (2014). Simultaneous targeting of IL-1 and IL-18 is required for protection against inflammatory and septic shock. Am. J. Respir. Crit. Care Med. *189*, 282–291. https://doi.org/10.1164/rccm.201308-1535OC.
34. Rittirsch, D., Huber-Lang, M.S., Flierl, M.A., and Ward, P.A. (2009). Immunodesign of experimental sepsis by cecal ligation and puncture. Nat. Protoc. *4*, 31–36. https://doi.org/10.1038/nprot.2008.214.
35. Hoffman, M., Kyriazis, I.D., Lucchese, A.M., de Lucia, C., Piedepalumbo, M., Bauer, M., Schulze, P.C., Bonios, M.J., Koch, W.J., and Drosatos, K. (2019). Myocardial Strain and Cardiac Output are Preferable Measurements for Cardiac Dysfunction and Can Predict Mortality in Septic Mice. J. Am. Heart Assoc. *8*, e012260. https://doi.org/10.1161/JAHA.119.012260.
36. Bonventre, J.V., and Yang, L. (2011). Cellular pathophysiology of ischemic acute kidney injury. J. Clin. Invest. *121*, 4210–4221. https://doi.org/10.1172/JCI45161.
37. Damman, K., and Testani, J.M. (2015). The kidney in heart failure: an update. Eur. Heart J. *36*, 1437–1444. https://doi.org/10.1093/eurheartj/ehv010.
38. Xu, J., Zhang, X., Pelayo, R., Monestier, M., Ammollo, C.T., Semeraro, F., Taylor, F.B., Esmon, N.L., Lupu, F., and Esmon, C.T. (2009). Extracellular histones are major mediators of death in sepsis. Nat. Med. *15*, 1318–1321. https://doi.org/10.1038/nm.2053.
39. Li, D., and Wu, M. (2021). Pattern recognition receptors in health and diseases. Signal Transduct. Targeted Ther. *6*, 291. https://doi.org/10.1038/s41392-021-00687-0.
40. Xu, J., Zhang, X., Monestier, M., Esmon, N.L., and Esmon, C.T. (2011). Extracellular histones are mediators of death through TLR2 and TLR4 in mouse fatal liver injury. J. Immunol. *187*, 2626–2631. https://doi.org/10.4049/jimmunol.1003930.
41. Huang, H., Evankovich, J., Yan, W., Nace, G., Zhang, L., Ross, M., Liao, X., Billiar, T., Xu, J., Esmon, C.T., and Tsung, A. (2011). Endogenous histones function as alarmins in sterile inflammatory liver injury through Toll-like receptor 9 in mice. Hepatology *54*, 999–1008. https://doi.org/10.1002/hep.24501.
42. Hoebe, K., Du, X., Georgel, P., Janssen, E., Tabeta, K., Kim, S.O., Goode, J., Lin, P., Mann, N., Mudd, S., et al. (2003). Identification of Lps2 as a key transducer of MyD88-independent TIR signalling. Nature *424*, 743–748. https://doi.org/10.1038/nature01889.
43. Watanabe, M., and Okada, T. (2018). Langendorff Perfusion Method as an Ex Vivo Model to Evaluate Heart Function in Rats. Methods Mol. Biol. *1816*, 107–116. https://doi.org/10.1007/978-1-4939-8597-5_8.
44. He, P., Ai, T., Yang, Z.H., Wu, J., and Han, J. (2021). Detection of necroptosis by phospho-MLKL immunohistochemical labeling. STAR Protoc. *2*, 100251. https://doi.org/10.1016/j.xpro.2020.100251.
45. Yang, G., Bao, P., Zhang, L., Lyu, Z., Zhou, B., Chen, K., Peng, S., Wang, Y., Yao, L., Zhou, Y., and Li, Y. (2014). Critical role of myeloid differentiation factor 88 in necrotizing enterocolitis. Pediatr. Res. *75*, 707–715. https://doi.org/10.1038/pr.2014.39.
46. Chen, H., Li, Y., Gu, J., Yin, L., Bian, F., Su, L., Hong, Y., Deng, Y., and Chi, W. (2018). TLR4-MyD88 pathway promotes the imbalanced activation of NLRP3/NLRP6 via caspase-8 stimulation after alkali burn injury. Exp. Eye Res. *176*, 59–68. https://doi.org/10.1016/j.exer.2018.07.001.
47. Harberts, E., Fishelevich, R., Liu, J., Atamas, S.P., and Gaspari, A.A. (2014). MyD88 mediates the decision to die by apoptosis or necroptosis after UV irradiation. Innate Immun. *20*, 529–539. https://doi.org/10.1177/1753425913501706.
48. Tang, Y., Harrington, A., Yang, X., Friesel, R.E., and Liaw, L. (2010). The contribution of the Tie2+ lineage to primitive and definitive hematopoietic cells. Genesis *48*, 563–567. https://doi.org/10.1002/dvg.20654.
49. Ogasawara, J., Watanabe-Fukunaga, R., Adachi, M., Matsuzawa, A., Kasugai, T., Kitamura, Y., Itoh, N., Suda, T., and Nagata, S. (1993). Lethal effect of the anti-Fas antibody in mice. Nature *364*, 806–809. https://doi.org/10.1038/364806a0.
50. Jodo, S., Kung, J.T., Xiao, S., Chan, D.V., Kobayashi, S., Tateno, M., Lafyatis, R., and Ju, S.T. (2003). Anti-CD95-induced lethality requires radioresistant Fcgamma RII+ cells. A novel mechanism for fulminant hepatic failure. J. Biol. Chem. *278*, 7553–7557. https://doi.org/10.1074/jbc.M211229200.
51. Van Hauwermeiren, F., Armaka, M., Karagianni, N., Kranidioti, K., Vandenbroucke, R.E., Loges, S., Van Roy, M., Staelens, J., Puimège, L., Palagani, A., et al. (2013). Safe TNF-based antitumor therapy following p55TNFR reduction in intestinal epithelium. J. Clin. Invest. *123*, 2590–2603. https://doi.org/10.1172/JCI65624.
52. Zou, Y., Zheng, Q., Jiang, B., Liu, Y., Xu, Y., Ma, L., Hu, Z., Wu, M., and Song, H. (2022). Deficiency of PPP6C protects TNF-induced necroptosis through activation of TAK1. Cell Death Dis. *13*, 618. https://doi.org/10.1038/s41419-022-05076-1.
53. Deng, B., Yang, D., Wu, H., Wang, L., Wu, R., Zhu, H., Huang, A., Song, J., Cai, T., Liu, S., et al. (2022). Ketamine inhibits TNF-alpha-induced cecal damage by enhancing RIP1 ubiquitination to attenuate lethal SIRS. Cell Death Dis. *8*, 72. https://doi.org/10.1038/s41420-022-00869-x.
54. Shi, F.L., Yuan, L.S., Wong, T.S., Li, Q., Li, Y.P., Xu, R., You, Y.P., Yuan, T., Zhang, H.R., Shi, Z.J., et al. (2023). Dimethyl fumarate inhibits necroptosis and alleviates systemic inflammatory response syndrome by blocking the RIPK1-RIPK3-MLKL axis. Pharmacol. Res. *189*, 106697. https://doi.org/10.1016/j.phrs.2023.106697.
55. Yu, S., Yang, H., Li, T., Pan, H., Ren, S., Luo, G., Jiang, J., Yu, L., Chen, B., Zhang, Y., et al. (2021). Efficient intracellular delivery of proteins by a multifunctional chimaeric peptide in vitro and in vivo. Nat. Commun. *12*, 5131. https://doi.org/10.1038/s41467-021-25448-z.
56. Cao, M., Chen, F., Xie, N., Cao, M.Y., Chen, P., Lou, Q., Zhao, Y., He, C., Zhang, S., Song, X., et al. (2018). c-Jun N-terminal kinases differentially regulate TNF- and TLRs-mediated necroptosis through their kinase-dependent and -independent activities. Cell Death Dis. *9*, 1140. https://doi.org/10.1038/s41419-018-1189-2.
57. Kokkinaki, D., Hoffman, M., Kalliora, C., Kyriazis, I.D., Maning, J., Lucchese, A.M., Shanmughapriya, S., Tomar, D., Park, J.Y., Wang, H., et al. (2019). Chemically synthesized Secoisolariciresinol diglucoside (LGM2605) improves mitochondrial function in cardiac myocytes and alleviates septic cardiomyopathy. J. Mol. Cell. Cardiol. *127*, 232–245. https://doi.org/10.1016/j.yjmcc.2018.12.016.
58. L'Heureux, M., Sternberg, M., Brath, L., Turlington, J., and Kashiouris, M.G. (2020). Sepsis-Induced Cardiomyopathy: a Comprehensive Review. Curr. Cardiol. Rep. *22*, 35. https://doi.org/10.1007/s11886-020-01277-2.
59. Abrams, S.T., Zhang, N., Manson, J., Liu, T., Dart, C., Baluwa, F., Wang, S.S., Brohi, K., Kipar, A., Yu, W., et al. (2013). Circulating histones are mediators of trauma-associated lung injury. Am. J. Respir. Crit. Care Med. *187*, 160–169. https://doi.org/10.1164/rccm.201206-1037OC.
60. Kim, J., Baalachandran, R., Li, Y., Zhang, C.O., Ke, Y., Karki, P., Birukov, K.G., and Birukova, A.A. (2022). Circulating extracellular histones exacerbate acute lung injury by augmenting pulmonary endothelial dysfunction via TLR4-dependent mechanism. Am. J. Physiol. Lung Cell Mol. Physiol. *323*, L223–L239. https://doi.org/10.1152/ajplung.00072.2022.

61. Reino, D.C., Pisarenko, V., Palange, D., Doucet, D., Bonitz, R.P., Lu, Q., Colorado, I., Sheth, S.U., Chandler, B., Kannan, K.B., et al. (2011). Trauma hemorrhagic shock-induced lung injury involves a gut-lymph-induced TLR4 pathway in mice. PLoS One *6*, e14829. https://doi.org/10.1371/journal.pone.0014829.

62. Wang, H., Bloom, O., Zhang, M., Vishnubhakat, J.M., Ombrellino, M., Che, J., Frazier, A., Yang, H., Ivanova, S., Borovikova, L., et al. (1999). HMG-1 as a late mediator of endotoxin lethality in mice. Science *285*, 248–251. https://doi.org/10.1126/science.285.5425.248.

63. Alhamdi, Y., Abrams, S.T., Cheng, Z., Jing, S., Su, D., Liu, Z., Lane, S., Welters, I., Wang, G., and Toh, C.H. (2015). Circulating Histones Are Major Mediators of Cardiac Injury in Patients With Sepsis. Crit. Care Med. *43*, 2094–2103. https://doi.org/10.1097/CCM.0000000000001162.

64. Kang, J.W., Kim, S.J., Cho, H.I., and Lee, S.M. (2015). DAMPs activating innate immune responses in sepsis. Ageing Res. Rev. *24*, 54–65. https://doi.org/10.1016/j.arr.2015.03.003.

65. Gong, T., Liu, L., Jiang, W., and Zhou, R. (2020). DAMP-sensing receptors in sterile inflammation and inflammatory diseases. Nat. Rev. Immunol. *20*, 95–112. https://doi.org/10.1038/s41577-019-0215-7.

66. Zhang, P., Liu, Y., Hu, L., Huang, K., Hong, M., Wang, Y., Fan, X., Ulevitch, R.J., and Han, J. (2021). NLRC4 inflammasome-dependent cell death occurs by a complementary series of three death pathways and determines lethality in mice. Sci. Adv. *7*, eabi9471. https://doi.org/10.1126/sciadv.abi9471.

67. Tang, Y., Wang, X., Li, Z., He, Z., Yang, X., Cheng, X., Peng, Y., Xue, Q., Bai, Y., Zhang, R., et al. (2021). Heparin prevents caspase-11-dependent septic lethality independent of anticoagulant properties. Immunity *54*, 454–467.e6. https://doi.org/10.1016/j.immuni.2021.01.007.

68. Coburn, B., Li, Y., Owen, D., Vallance, B.A., and Finlay, B.B. (2005). Salmonella enterica serovar Typhimurium pathogenicity island 2 is necessary for complete virulence in a mouse model of infectious enterocolitis. Infect. Immun. *73*, 3219–3227. https://doi.org/10.1128/IAI.73.6.3219-3227.2005.

69. Ha, T.W., Oh, B., and Kang, J.O. (2020). Electrocardiogram Recordings in Anesthetized Mice using Lead II. J. Vis. Exp. *20*, 1–13. https://doi.org/10.3791/61583.

70. Hua, F., Wu, Z., Yan, X., Zheng, J., Sun, H., Cao, X., and Bian, J.S. (2018). DR region of Na(+)-K(+)-ATPase is a new target to protect heart against oxidative injury. Sci. Rep. *8*, 13100. https://doi.org/10.1038/s41598-018-31460-z.

71. Bell, R.M., Mocanu, M.M., and Yellon, D.M. (2011). Retrograde heart perfusion: the Langendorff technique of isolated heart perfusion. J. Mol. Cell. Cardiol. *50*, 940–950. https://doi.org/10.1016/j.yjmcc.2011.02.018.

72. Agnieszka Krzyzanowska, Y.M., Avendaño, C., and Jose Piedras, M. (2010). Evaluation of Evans Blue extravasation as a measure of peripheral inflammation. Protocol Exchange *209*, 1–12. https://doi.org/10.1038/protex.2010.209.

STAR★METHODS

KEY RESOURCES TABLE

REAGENT or RESOURCE	SOURCE	IDENTIFIER
Antibodies		
anti-*p*-MLKL (S345) antibody	Abcam	Cat# ab196436; RRID: AB_2687465
anti-cleaved caspase8 antibody	Cell Signaling Technology	Cat# 9429S; RRID: AB_2068300
anti-histone3 antibody	Proteintech	Cat# 17168-1-AP; RRID: AB_2716755
anti-mouse/rabbit IgG	Vector laboratories	Cat# MP-7500; RRID: AB_2336534
biotinylated anti-mouse/rabbit IgG	Vector laboratories	Cat# BA-1400; RRID: AB_2336187
horseradish peroxidase (HRP)-conjugated goat anti-rabbit antibody	Thermo Fisher Scientific	Cat# 31460; RRID: AB_228341
Chemicals, peptides, and recombinant proteins		
mouse TNF-α (referred as TNF in the manuscript)	Novoprotein	Cat# CF09
calf thymus histones	Sigma-Aldrich	Cat# H5505; CAS: 9064-47-5
bovine serum albumin (BSA)	Sigma-Aldrich	Cat# A1933; CAS: 9048-46-8
lipopolysaccharide (LPS)	Sigma-Aldrich	Cat# L3024
Isoflurane	Veteasy	Cat# R510-22-8
Penicillin	Sangon Biotech	Cat# A600135; CAS: 69-57-8
mouse IL-6 ELISA kit	eBioscence	Cat# 88-7064-88
mouse IL-1β ELISA kit	Proteintech	Cat# KE10003
mouse IL-18 ELISA kit	Elabsciences	Cat# E-EL-M0730
mouse IFN-β ELISA kit	Elabsciences	Cat# E-EL-M0033
mouse IFN-γ ELISA kit	eBioscence	Cat# BMS609
mouse IL-22 ELISA kit	BioLegend	Cat# 436304
mouse cTn-1 ELISA kit	Cusabio	Cat# CSB-E08421m
Hematoxylin	MXB Biotechnologies	Cat# CTS-1096
Eosin	ZSGB-BIO	Cat# ZLI-9613
periodic acid	Thermo Fisher Scientific	Cat# 87007
schiff reagent	Abcam	Cat# ab150680
sodium citrate	Sigma	Cat# W302600; CAS: 6132-04-3
tween 20	Sigma	Cat# P1379-6X; CAS: 9005-64-5
normal horse serum	Vector laboratories	Cat# S-2012-50
FITC-conjugated wheat germ agglutinin (FITC-WGA)	Invitrogen	Cat# W11261
Hoechst 33258	Thermo Fisher Scientific	Cat# H3569
NuPAGE™ 12% Bis-Tris Protein Gel	Invitrogen	Cat# NP0343BOX
polyvinylidene difluoride (PVDF) membrane	Millipore	IPVH00010
ECL Western Blotting Detection Reagent	Ncmbio	Cat# P10300
enhanced chemiluminescence system	GE Healthcare	Amersham Imager 600
coomassie blue	Sangon Biotech	Cat# A600038; CAS: 6104-58-1
ultrasonic couplant	Jinya	Cat# TM-100
methanol	Sigmac	Cat#322415; CAS: 67-56-1
prostaglandin E2	Cayman Chemical	Cat# 314010; CAS: 34210-10-1
prostaglandin D2	Cayman Chemical	Cat# 12010; CAS: 41598-07-6
prostaglandin F2α	Cayman Chemical	Cat# 16010; CAS: 551-11-1
thromboxane B2	Cayman Chemical	Cat# 19030; CAS: 54397-85-2
leukotriene B4	Cayman Chemical	Cat# 20110; CAS: 71160-24-2
lipoxin A4	Cayman Chemical	Cat# 90410; CAS: 89663-86-5

(*Continued on next page*)

Continued

REAGENT or RESOURCE	SOURCE	IDENTIFIER
5-HETE	Cayman Chemical	Cat# 34230; CAS: 70608-72-9
12-HETE	Cayman Chemical	Cat# 34570; CAS: 54397-83-0
15-HETE	Cayman Chemical	Cat# 34720; CAS: 54845-95-3
5,12-HETE	Cayman Chemical	Cat# 35260; CAS: 79056-01-2
Dithiothreitol (DTT)	Sigma-Aldrich	Cat# D0632; CAS: 3483-12-3
Iodoacetamide (IAA)	Sigma-Aldrich	Cat# I1149; CAS: 144-48-9
Formic acid (FA)	Sigma-Aldrich	Cat# 695076; CAS: 64-18-6
triethylammonium bicarbonate	Sigma-Aldrich	Cat# 18597; CAS: 64-18-6
Evans Blue	Sigma-Aldrich	Cat# E2129; CAS: 314-13-6
ATP Assay Kit	Beyotime	Cat# S0027
chloroform	Sigma-Aldrich	Cat#: C2432; CAS: 67-66-3
Deposited data		
Serum mass spectrometry data	This paper	PRIDE database, ProteomeXchange identifiers: PXD048104
Experimental models: Organisms/strains		
C57BL/6J mice	Jackson Laboratory	Strain # 000664
Vav$^{cre/-}$ mice	Jackson Laboratory	Strain # 008610
Tie2$^{cre/-}$ mice	Jackson Laboratory	Strain # 008863
Tlr4$^{-/-}$ mice	Jackson Laboratory	Strain # 029015
Tlr9$^{-/-}$ mice	Jackson Laboratory	Strain # 014534
Trif$^{-/-}$ mice	Jackson Laboratory	Strain # 005037
Myd88 $^{fl/fl}$ mice	Jackson Laboratory	Strain # 008888
Mlkl$^{-/-}$ mice	Wu et al., 2013	N/A
Rip3$^{-/-}$ mice	Newton, K., 2004	N/A
Caspase8$^{-/-}$ mice	Zhang et al., 2021	N/A
Caspase8$^{fl/fl}$ mice	Beisner et al., 2005	N/A
α*MHC*$^{cre/-}$ mice	Wang et al., 2005	N/A
Myd88$^{-/-}$ mice	This paper	N/A
Tlr2$^{-/-}$ mice	This paper	N/A
Tnfr1$^{fl/fl}$ mice	This paper	N/A
Rip3$^{fl/fl}$ mice	This paper	N/A
Oligonucleotides		
genotyping primer for *Mlkl*$^{-/-}$ mice #1: 5′-agcccaaagaggcagcacaaatc -3′	This paper	N/A
genotyping primer for *Mlkl*$^{-/-}$ mice #2: 5′-aaacttccaaatatgggacttcttg-3′	This paper	N/A
genotyping primer for *Rip3*$^{-/-}$ mice #1: 5′-cgctttagaagccttcaggttgac-3′	This paper	N/A
genotyping primer for *Rip3*$^{-/-}$ mice #2: 5′-gcaggctctggtgacaagattcatgg-3′	This paper	N/A
genotyping primer for *Rip3*$^{-/-}$ mice #3: 5′-ccagaggccacttgtgtagcg-3′	This paper	N/A
sgRNAs used to target *Myd88* exons #1: 5′-cggccgccacgggcgtccga-3′	This paper	N/A
sgRNAs used to target *Myd88* exons #2: 5′-cccttggtcgcgcttaacgt-3′	This paper	N/A
genotyping primer for *Myd88*$^{-/-}$ mice #1: 5′-ggctggcaggagacttaa-3′	This paper	N/A
genotyping primer for *Myd88*$^{-/-}$ mice #2: 5′-acttcagctccttcagtatatc-3′	This paper	N/A

(*Continued on next page*)

Continued

REAGENT or RESOURCE	SOURCE	IDENTIFIER
sgRNAs used to target *Tlr2* exons #1: 5′-ggaaaggggcccgaaccagg-3′	This paper	N/A
sgRNAs used to target *Tlr2* exons #2: 5′-ccacaagcgggacttcgttc-3′	This paper	N/A
genotyping primer for *Tlr2*$^{-/-}$ mice #1: 5′-cgccctttaagctgtgtctc-3′	This paper	N/A
genotyping primer for *Tlr2*$^{-/-}$ mice #2: 5′-ttggctcttctggatcttgg-3′	This paper	N/A
genotyping primer for *Tlr2*$^{-/-}$ mice #3: 5′-acccaaaacacttcctgctg-3′	This paper	N/A
genotyping primer for *Tlr4*$^{-/-}$ mice #1: 5′-gcaagtttctatatgcattctc-3′	This paper	N/A
genotyping primer for *Tlr4*$^{-/-}$ mice #2: 5′-cagggctgctttcctcctag-3′	This paper	N/A
genotyping primer for *Tlr4*$^{-/-}$ mice #3: 5′-aggcattgtgttagtacagga-3′	This paper	N/A
genotyping primer for *Tlr9*$^{-/-}$ mice #1: 5′-caccaatgcctttcagaacc-3′	This paper	N/A
genotyping primer for *Tlr9*$^{-/-}$ mice #2: 5′-gccatctgagcgtgtacttg-3′	This paper	N/A
genotyping primer for *Trif*$^{-/-}$ mice #1: 5′-acctcagcctctcattattc-3′	This paper	N/A
genotyping primer for *Trif*$^{-/-}$ mice #2: 5′-gtccaactaatagccactgt-3′	This paper	N/A
genotyping primer for *Myd88* $^{fl/fl}$ mice #1: 5′-gttgtgtgtgtccgaccgt-3′	This paper	N/A
genotyping primer for *Myd88* $^{fl/fl}$ mice #2: 5′-gtcagaaacaaccaccaccatgc-3′	This paper	N/A
genotyping primer for *Rip3*$^{fl/fl}$ #1: 5′-gaaagaaagtcgggattgg-3′	This paper	N/A
genotyping primer for *Rip3*$^{fl/fl}$ mice #2: 5′-agagtagtgcctgctgtt-3′	This paper	N/A
genotyping primer for *Caspase8*$^{fl/fl}$ mice #1: 5′-ataattcccccaaatcctcgcatc-3′	This paper	N/A
genotyping primer for *Caspase8*$^{fl/fl}$ mice #2: 5′-ggctcactcccagggcttcct-3′	This paper	N/A
genotyping primer for *Tnfr1*$^{fl/fl}$ mice #1: 5′-gttggactaggttgcttaga-3′	This paper	N/A
genotyping primer for *Tnfr1*$^{fl/fl}$ mice #2: 5′-gagcaccatcacctacataa-3′	This paper	N/A
genotyping primer for *Vav*$^{cre/-}$ #1: 5′-agatgccaggacatcaggaacctg-3′	This paper	N/A
genotyping primer for *Vav*$^{cre/-}$ mice #2: 5′-atcagccacaccagacacagagat -3′	This paper	N/A
genotyping primer for α*MHC*$^{cre/-}$ mice #1: 5′-atgacagacagatccctcctatctcc-3′	This paper	N/A
genotyping primer for α*MHC*$^{cre/-}$ mice #2: 5′-ctcatcactcgttgcatcatcatcgac-3′	This paper	N/A
genotyping primer for *Tie2*$^{cre/-}$ mice #1: 5′-ccacacacgtgcacatatagа-3′	This paper	N/A
genotyping primer for *Tie2*$^{cre/-}$ mice #2: 5′-gcgtttaagtaatgggatggtc-3′	This paper	N/A
Software and algorithms		
GraphPad Prism 10	GraphPad Software Inc.	https://www.graphpad.com/

(*Continued on next page*)

Continued

REAGENT or RESOURCE	SOURCE	IDENTIFIER
Adobe Illustrator	Adobe Inc.	N/A
ImageJ	NIH	https://imagej.nih.gov/ij/
ZEN3.9	ZEN Microscopy Software	https://www.zeiss.com.cn/microscopy/products/microscope-software/zen.html
PEAKS Studio X Pro	Bioinformatics Solutions, Inc., Waterloo	https://www.bioinfor.com/download-peaks-studio/
EMapRecord 5.0 software	MapingLab Ltd., UK	https://www.mappinglab.cn/product/emaprecord-acquisition
SPSS (version 27.0)	IBM	https://www.ibm.com/support/pages/downloading-ibm-spss-statistics-27
Other		
absorbance microplate reader	BioTek	Cat# ELX800
fluorescence microscope	Olympus Corporation	Cat# IX51
multiple-channel physiological signal collecting and processing instrument	Chengdu Instrument factory	Cat# RM6240B
high-resolution echocardiography system	Visual Sonics	Cat# Vevo 2100
Labconco CentriVap®	Labconco	Cat# 7970010
ultrahigh-pressure nanoflow chromatography system (Elute UHPLC)	Bruker	
hybrid TIMS quadrupole time-of-flight mass spectrometer (TimsTOF Pro)	Bruker	
32-channel electrophysiological mapping system	MappingLab	Cat# EMS32-USB-1003/1003CS
automatic biochemical analyzer	Mindray	Cat# BS240-VET

EXPERIMENTAL MODEL AND STUDY PARTICIPANT DETAILS

Mice

All the mice were housed and fed in a specific pathogen-free facility on a 12-h light-dark cycle (lights on 8 a.m. to 8 p.m.) at the Laboratory Animal Center of Xiamen University. The room temperature was 22°C–24°C, and the room humidity was 50–70%. All the mice were backcrossed with wild-type C57BL/6J mice for at least 6 generations. Unless stated otherwise, both male and female mice (10–12 weeks old) were used in this study, and the experimental and control animals were cohoused. Mice that reached the ethical endpoint (body temperature below 23.6°C) were euthanized with carbon dioxide.[66] All the mouse experiments were approved by the Animal Care and Use Committee of Xiamen University (XMULAC20210072).

METHOD DETAILS

TNF-induced SIRS

Age- and sex-matched mice (10–12 weeks) were injected intravenously with mouse TNF-α (referred as TNF in the manuscript) diluted in endotoxin-free PBS at a dose of 0.4 μg/g (LD_{100}) unless especially indicated (0.2 μg/g as LD_{50}). Rectal temperature was measured every 3 or 4 h as indicated in the figure legends.

For histone or BSA administration, purified calf thymus histones or BSA were injected intravenously 4 h after TNF injection at a dose of 20 μg/g. Mice were sacrificed at the indicated time or when the body temperature dropped below 23.6°C according to ethical guidelines.

LPS-induced sepsis

Age- and sex-matched mice (10–12 weeks) were injected intraperitoneally with LPS diluted in endotoxin-free PBS at a dose of 25 μg/g.[67] The mice were sacrificed at the indicated time or when the body temperature dropped below 23.6°C according to the ethical guidelines.

Cecectomy

Cecectomy was performed as described previously.[30] Briefly, 5-7 weeks-old mice were anesthetized continuously with isoflurane. The abdomen was shaved, and the skin was disinfected with 75% alcohol. A 0.5 to 1.0 cm incision was made along the lower abdomen. The cecum was gently exteriorized and placed on a sterile drape rinsed in saline. The cecum was then ligated at the

ileocecal junction and excised carefully. Sterile PBS was then used to irrigate the residual ingesta on the incision surface to avoid leakage of the cecal contents into the peritoneal cavity. After surgery, the exteriorized intestines were placed back in the abdominal cavity, and the mice were intraperitoneally injected with 0.5 mL of 10 mg/kg penicillin to prevent infection. Finally, the abdominal muscle layers and skin were separately sutured with 4-0 sutures, and 1 mL of saline was administered via subcutaneous injection into the neck. Each surgery was completed within 6 min, and the intestine was kept moist with saline during the whole process. In the sham group, the same surgical procedure, including exteriorization of the cecum for 2 min, was performed except ligation at the ileocecal junction and cecum removal.

All the surgical mice were kept on a thermostatic blanket at approximately 37°C for 2 h for recovery, and the surgical incision sites were monitored daily for 2 weeks.

Detection of bacteria in blood

The animals were anesthetized with 2% isoflurane, and blood was obtained via cardiac puncture. The samples were serially diluted in sterile PBS, blood lysates were cultured on agar plates without antibiotics for 48–72 h at 37°C, and colonies were counted.

Collection of serum

Blood was collected from the retro-orbital vein of mice and incubated at 37°C for 30 min. The coagulated blood was centrifuged at 2000x g for 20 min, and the supernatant was collected. The collected supernatant was centrifuged at 5000x g for another 5 min, and the supernatant was carefully collected as the serum sample. Centrifugation was performed at 4°C, and the serum samples were aliquoted and stored in a −80°C ultralow temperature freezer for future analysis.

ELISA

The serum concentrations of inflammatory cytokines (IL-6, IL-1β, IL-18, IFN-β, IFN-γ, and IL-22) or biomarkers (cTn-1) were measured following the manufacturer's protocol. An absorbance microplate reader was used to measure the absorbance for ELISA. The ELISA kits used in this study were as follows: mouse IL-6 ELISA kit, mouse IL-1β ELISA kit, mouse IL-18 ELISA kit, mouse IFN-β ELISA kit, mouse IFN-γ ELISA kit, mouse IL-22 ELISA kit and mouse cTn-1 ELISA kit.

Histopathology

Mice were euthanized with carbon dioxide, and tissues or organs were soaked in 10% formalin, dehydrated through graded alcohols and xylene and embedded in paraffin wax. The paraffin samples were sectioned at a thickness of 5 μm. Fixed sections were processed and then stained with hematoxylin and eosin (H&E) based on a routine protocol. The degree of cecal damage was assessed by a method described previously,[68] and the average score of four fields per sample was used as the damage score.

For periodic acid-Schiff staining, kidney tissue sections were first stained with 1% periodic acid, then stained with Schiff reagent and hematoxylin. The proportion of renal tubule damage in 8 fields per sample was determined.

For immunohistochemical staining, as described previously,[44] paraffin-embedded sections were incubated in antigen retrieval buffer (10 mmol/L sodium citrate buffer (pH 6.0) containing 0.05% Tween 20. The sections were blocked with 2.5% normal horse serum. Some sections were incubated with an anti-*p*-MLKL (S345) antibody (Abcam, dilution 1:1500) at 4°C overnight, followed by antibody detection using the Horse Anti-Mouse/Rabbit IgG (Vector laboratories) 1h at room temperature. Some sections were incubated with anti-cleaved Caspase8 antibody (CST, dilution 1:200) at 4°C overnight, followed by antibody detection using biotinylated anti-mouse/rabbit IgG (Vector laboratories) for 1h at room temperature.

Representative images were captured and processed using identical settings on a Leica DM2500 microscope at Xiamen University.

Wheat germ agglutinin (WGA) staining

Paraffin-embedded sections (5 μm thick) were stained with FITC-conjugated wheat germ agglutinin (WGA, 10ug/mL) to visualize the cell membrane, and Hoechst 33258 was used to stain the nuclei. Sections were observed under a fluorescence microscope (20×), and images were captured. The areas of more than 150 myocytes were counted and averaged to obtain the cardiomyocyte size for each group. The investigators were blinded to the groups during WGA staining and determination of the myocyte size.

Western blotting

Serum samples were diluted ten times and mixed with an equal volume of 2x SDS sample buffer. A total of 20 μL per sample was separated on a NuPAGE 12% Bis-Tris Protein Gel (Invitrogen) and then transferred to a polyvinylidene difluoride (PVDF) membrane (Millipore). The membrane was then blocked with 5% milk for 1 h at room temperature and then incubated with Histone3 antibody (Proteintech, dilution 1:1000) overnight at 4°C. After being washed 3 times with 1x TBST buffer, the membrane was incubated with a horseradish peroxidase (HRP)-conjugated goat anti-rabbit antibody (Thermo, dilution 1:10000) for 1 h at room temperature. The membrane was then washed 3 times. The protein bands were visualized with ECL Western Blotting Detection Reagent, and images were acquired with an enhanced chemiluminescence system. Another 20 μL per sample was separated on a NuPAGE 12% Bis-Tris Protein Gel and stained with Coomassie blue to show the total serum protein concentration as loading controls.

Electrocardiography (ECG)

Electrocardiograms were recorded as described previously.[69] Briefly, mice were lightly anesthetized with 1% isoflurane and placed on a warm platform. Electrodes were positioned on the sole of each foot for lead II ECG. Electrocardiogram waveforms were recorded by an RM6240B multiple-channel physiological signal collecting and processing instrument.

Echocardiography

Mouse cardiac echocardiography was performed with a high-resolution echocardiography system following a previously described protocol.[70] Briefly, the mouse chest was depilated with depilatory cream, and the mice were anesthetized with inhaled isoflurane and maintained at 37°C on a heating pad. An ultrasonic couplant was smeared on the chest skin, and real-time ultrasonography was performed with a detector. All measurements were the average over six consecutive cardiac cycles. The following parameters were measured and calculated by an echocardiography system: left ventricular fractional shortening (LVFS), left ventricular ejection fraction (LVEF), heart rate (HR), cardiac output (CO), left ventricular internal dimension (LVID) in diastole and systole (LVID, d and LVID, s, respectively), left ventricular end diastolic and systole volume (LV vol, d and LV vol, s, respectively), left ventricular posterior wall (LVPW) thickness in diastole and systole (LVPW, d and LVPW, s, respectively), and the interventricular septum (IVS) dimension in diastole and systole (IVS, d and IVS, s, respectively).

Cardiac electrolyte and ATP analysis

To prepare samples for analysis, the blood in the heart was quickly cleared, and the heart was rapidly frozen using liquid nitrogen. For electrolyte analysis, the frozen cardiac tissues were lysed, and the concentrations of Na^+, K^+, and bicarbonate in the lysate were measured using an automatic biochemical analyzer (BS240-VET, Mindray).

For ATP analysis, 100 mg of frozen cardiac tissue was added to pre-cooled methanol (1 mL). The tissue was ground, and the lysate was mixed with chloroform (1 mL) and ddH_2O (400 μL), followed by vortexing for 20 s. After centrifugation at 15,000 g for 15 min at 4°C, 450 μL of the aqueous phase was collected and dried at 4°C. The sediment was resuspended in 20–40 μL of ddH_2O, and the ATP concentration was measured using an ATP Assay Kit (S0027, Beyotime).

Eicosanoid level analysis

One hundred microlitres of collected serum was mixed with 500 μL of cold methanol, stored at −80°C overnight, and then centrifuged at 15000x g for 10 min. The supernatant was transferred to a new tube and lyophilized in Labconco CentriVap. The lyophilized powder was stored at −80°C and resolved with 70% methanol for analysis as needed. Eicosanoid and docosanoid levels in the samples were quantified by the QTRAP-6500 plus system (SCIEX). Synthetic standards were purchased from Cayman Chemical (prostaglandin E2, prostaglandin D2, prostaglandin F2α, thromboxane B2, leukotriene B4, lipoxin A4, 5-HETE, 12-HETE, 15-HETE, 5, 12-HETE).

Protein digestion and iTRAQ labeling

Collected serum samples were denatured with 8 M urea. Disulfide bonds were reduced by 10 mM DTT, and the samples were alkylated by 40 mM IAA. The samples were diluted with 50 mM NH_4HCO_3 to achieve a final urea concentration of 2 M. Trypsin was added at a protein: trypsin ratio of 50:1 to digest the serum proteins for 12–18 h at 37°C. FA was then added to the peptide mixture to a final concentration of 1%. The acidified mixture was then centrifuged at 12000 rpm, and the supernatants were separated on SepPak C18 columns (Waters). The desalted peptides were divided into 100 μg aliquots, lyophilized to complete dryness, and stored at −80°C for future analysis. The peptides were labeled with iTRAQ reagents (Applied Biosystems, Foster City) according to the manufacturer's instructions (400 μg in total for 4 plex). Briefly, 100 μg aliquots of dried peptides were reconstituted with 30 μL of 0.5 M triethylammonium bicarbonate. One tube of iTRAQ reagent (114, 115, 116, or 117) was reconstituted with 70 μL of ethanol and added to each peptide solution. The reaction was allowed to proceed for 1 h at room temperature. Derivatized peptides were combined, dried by vacuum centrifugation, and desalted on SepPak C18 columns (Waters). The iTRAQ-labeled peptides were lyophilized to complete dryness and stored at −80°C until further analysis. The labeled peptides were fractionated by using SCX StageTips.

TimsTOF Pro mass spectrometry

Liquid chromatography was performed on an ultrahigh-pressure nanoflow chromatography system. Peptides were separated on a reversed-phase column (40 cm × 75 μm i.d.) packed with 1.8 μm 120 Å C18 material (Welch, Shanghai) at 50°C with a pulled emitter tip. Solution A was 0.1% FA in H_2O, and solution B was 0.1% FA in ACN. The gradient time was 60 min, and the total run time was 75 min, which included washing and equilibration. Peptides were separated with a linear gradient of 0%–5% solution B within 5 min, followed by an increase to 30% solution B within 55 min and to 35% solution B within 5 min, a washing step with 95% solution B and re-equilibration. The liquid chromatography system was coupled online to a hybrid TIMS quadrupole time-of-flight mass spectrometer via a CaptiveSpray nanoelectrospray ionization source. Data-dependent data acquisition was performed in PASEF mode with 10 PASEF scans per topN acquisition cycle. Singly charged precursors were excluded by their position in the m/z-ion mobility plane, and precursors that reached a 'target value' of 20,000 a.u. were dynamically excluded for 0.4 min. All the raw files (.d) were analyzed by PEAKS Studio X Pro (Bioinformatics Solutions, Inc., Waterloo). The proteome of *M. musculus* (UP000000589), which included common contaminants and decoys and contained 34269 entries, was downloaded from UniProt (reviewed sequences only). Carbamidomethylation of cysteines (+57.02 Da) and iTRAQ-modified N-terminal and lysine side chains of tryptic peptides (+304.2 Da)

were selected as fixed modifications, and oxidation of methionine (+15.99 Da) and iTRAQ-modified tyrosine (+304.2 Da) were set as variable modifications for the analysis. Only 1 missed cleavage was allowed, and the majority of peptides had no missed cleavages. The precursor and fragment mass tolerances were set to 15 ppm and 0.05 Da, respectively.

Langendorff perfusion experiments

Langendorff perfusion experiments were carried out following a widely used protocol.[71] Tyrode's perfusion buffer (128.2 mM NaCl, 4.7 mM KCl, 1.05 mM $MgCl_2$, 1.19 mM KH_2PO_4, 1.3 mM $CaCl_2$, 20 mM $NaHCO_3$ and 11.1 mM glucose, pH = 7.4) was equilibrated with 5% CO_2 and 95% O_2 at 37°C for at least 30 min before use. Mice were injected intraperitoneally with heparin (120 IU per mouse) and anesthetized via inhaled isoflurane (2%) 15 min after heparin injection. Mouse hearts were then rapidly excised in chilled Tyrode's perfusion buffer. After being cannulated on a Langendorff perfusion apparatus, the heart was retrogradely perfused via the aorta with Tyrode's perfusion buffer at 37°C. A 32-channel multi-electrical array was tightly attached to the left ventricle to record ECG data *ex vivo*, and the data were recorded and analyzed with EMapRecord 5.0 software. Drugs were sequentially added to the perfusion buffer as described in the manuscript at the following final concentrations: PBS: 0.1%; TNF: 0.3 μg/mL; and histones: 5 μg/mL.

Vascular permeability assay

Vascular permeability was measured by an Evans Blue method.[72] Evans Blue solution (4 mg/mL) was injected intravenously at a dose of 40 μg/g 7.5 h after TNF administration. Thirty minutes later, mice were anesthetized via 1% isoflurane inhalation, and the heart was flushed with 1x PBS through the apex. Place the heart in aluminum foil in an oven at 56°C for two days to dry. Then, the heart sample was immersed with formamide at a dose of 8 mL per 1g of dry tissue in an Eppendorf tube, and subsequently placed into the oven at 56°C for another two days. The amount of extracted Evans Blue dye in formamide was assessed by spectrophotometry at 620 nm on an absorbance microplate reader.

QUANTIFICATION AND STATISTICAL ANALYSIS

Statistical analysis was performed with GraphPad Prism (version 8.02) and SPSS (version 27.0). An unpaired two-tailed Student's *t* test was used to compare differences between the indicated groups except for differences in cecal damage severity and renal damage severity, which were analyzed with the Wilcoxon signed-rank test, and the *p* value was calculated. Mouse survival is presented as a Kaplan-Meier plot and was analyzed with a log rank (Mantel–Cox) test. The data are presented as the mean ± SEM. The significance of differences between groups is indicated in the figure as follows: ns: $p \geq 0.05$; *: $p < 0.05$; **: $p < 0.01$; ***: $p < 0.001$; ****: $p < 0.0001$. All the images presented in the manuscript are representative of a minimum of three independent experiments. The investigators were blinded to the groups during the experiments and outcome assessment.